On-the-fly simulations of transient absorption pump-probe spectra: combining mapping dynamics with doorway-window protocoal

Zhaofa Li,[†,§] Jiawei Peng,[†,§] Yifei Zhu,[‡,§] Chao Xu,[‡,§] Maxim F. Gelin,[*,¶] Feng Long Gu,[*,‡,§] and Zhenggang Lan[*,‡,§]

†*School of Chemistry, South China Normal University, Guangzhou 510006, P. R. China*

‡*SCNU Environmental Research Institute, Guangdong Provincial Key Laboratory of Chemical Pollution and Environmental Safety, School of Environment, South China Normal University, Guangzhou 510006, P. R. China*

¶*School of Science, Hangzhou Dianzi University, Hangzhou 310018, China*

§*MOE Key Laboratory of Environmental Theoretical Chemistry, South China Normal University, Guangzhou 510006, P. R. China*

E-mail: maxim@hdu.edu.cn; gu@scnu.edu.cn; zhenggang.lan@m.scnu.edu.cn

Abstract

We have developed an ab initio protocol for the simulation of transient-absorption (TA) pump-probe (PP) signals of realistic polyatomic systems. The protocol is based on interfacing the doorway-window representation of spectroscopic signals with the on-the-fly mapping Hamiltonian dynamics approach at the symmetrical quasi-classical/Meyer-Miller (SQC/MM) level. The methodology is applied to the simulation TA PP signals of two molecular systems, azobenzene and cis-hepta-3,5,7-trieniminium cation (PSB4). For both molecules, the TA PP spectra were demonstrated to give a direct fingerprint of the excited state wavepacket dynamics and internal conversion, as well as permit the monitoring of the isomerization pathways en route to the final photoproducts.

1 Introduction

Photoinduced nonadiabatic processes play essential roles in photophysics, photochemistry, and photobiology.[1,2] Studying of nonadiabatic dynamics shapes our understanding of many fundamental photoinduced phenomena, such as photosynthesis,[3–6] photostability,[7,8] and photoisomerization.[9–11] Modern femtosecond spectroscopy offers a variety of experimental tools for the visualization of the ultrafast nonadiabatic dynamics in photoinduced excited-state processes.[12–16] Among them, transient absorption (TA) pump-probe (PP) spectroscopy is one of the most widely employed and powerful experimental techniques.[16–19]

The impressive progress in experimental femtosecond spectroscopy stimulates rapid development of accurate (especially, ab initio) methods of simulations of spectroscopic signals, see, for example, the original works[20–28] and recent reviews.[29–34] The signals are usually calculated by using the nonlinear response-function (NRF) approach, in which interactions of molecules with laser fields are assumed to be weak and treated in the lowest order of perturbation theory.[35] However, a direct computation of the NRFs is tedious, especially for complex multidimensional molecular systems.[29–34] The doorway-window (DW) approximation provides a practical alternative which substantially alleviates the computational costs.[32,36,37] The DW representation of TA PP signals hinges on two assumptions: (1) the pump and probe pulses are well separated in the time domain; (2) durations of both pulses are much shorter than the time scale of the system evolution. Under the DW approximation, evaluation of the TA PP signal is decomposed into three steps: evaluation of the doorway operator which describes interaction of the system with the pump pulse, field-free propagation of the doorway wavepacket, convolution of the doorway wavepacket with the window operator which describes interaction of the system with the probe pulse. In other words, calculation of TA PP signals is reduced to the propagation of the electronic ground-state and excited-state wavepackets.

A variety of theoretical approaches of different complexity and accuracy are available for the nonadiabatic excited-state wavepacket propagation in complex molecular systems. On the one hand, a fully quantum evaluation of the Hamiltonian dynamics[1,2,38–40] or the dissipative dynamics[41–44] is certainly possible, but these methods are suitable only for the excitonic or linear-vibronic-coupling Hamiltonians. On the other hand, great efforts have been devoted to development of mixed quantum-classical trajectory-based or Gaussian-wavepacket-based propagation schemes.[45–49] In the commonly used trajectory surface hopping (TSH) method,[50] for example, the nuclear propagation is governed by classical mechanics and the electronic evolution is described by quantum mechanics. These trajectory-based approaches are especially attractive: Firstly, they usually require only the local information on the potential energy surface along the trajectory. Secondly, they can be conveniently interfaced with ab initio electronic structure calculations. This turns the on-the-fly trajectory methods into a powerful and efficient tool for the simulation of the nonadiabatic dynamics of realistic molecular systems undergoing arbitrary atomic motions.[47–56]

Recently considerable efforts have been devoted to the implementation of these on-the-fly trajectory-based dynamics methods for the simulations of time-resolved spectroscopic signals of model and realistic systems by using the NRFs and DW formalisms, see the original papers[28,57–59] and the reviews.[29–34] For example, the ab initio TSH-DW methodology has been developed in Ref.[60] However, it is well known that all mixed quantum-classical dynamics methods may suffer from a number of deficiencies and restrictions. For instance, the famous fewest-switches surface-hopping algorithm (FSSH) does not properly describe electronic decoherence.[46,61–63] It is thus worthwhile to explore a possibility of using alternative quantum-classical methods[64] for the on-the-fly evaluation of nonlinear spectroscopic responses, in the hope that these methods will better reproduce the effects related to electronic and vibrational coherences.

A promising and viable alternative to trajectory-based nonadiabatic simulations is provided by the mapping Hamiltonian framework. Instead of running the dynamics generated by the original electron-vibrational Hamiltonian, the mapping Hamiltonian is used in which electronic degrees of freedom (DoF) are transformed into coupled continuous classical degrees of freedom DoFs.[65–69] This provides a starting point for a family of various trajectory-based dynamics approaches.[70–78] In the well-known Meyer-Miller (MM) mapping model (frequently, it is referred to as the Meyer-Miller-Stock-Thoss model[79]), the quantum Hamiltonian containing N coupled electronic states is mapped into the Hamiltonian containing N coupled harmonic oscillators. This mapping procedure is founded on Schwinger's theory of angular momentum.[68,79] Among different MM mapping schemes, the symmetrical quasi-classical (SQC) variant provides an effective way to simulate nonadiabatic processes.[80–84] Several benchmark calculations have shown that the SQC/MM method gives a reasonably accurate description at affordable computational costs.[70,85–89] In the SQC/MM simulations, the triangle windowing protocol and the adjusted γ correction are always recommended.[90–94] After convincing demonstrations of performing mapping dynamics in on-the-fly,[71,95,96] the SQC/MM and other mapping approaches have been successfully applied to realistic polyatomic systems.[94,97–99]

Several decades ago, the mapping approach was used for the calculation of spectroscopic signals.[100–103] Nowadays, the methodology has actively been used and advanced.[104–109] Yet it is rather demanding to employ the mapping method for the calculation of three-time NRFs, owing to the necessity to do multiple forward and backward propagations on a three-dimensional time grid. Hence the methodology is usually applied to model systems, because its use for the on-the-fly spectroscopic simulations of realistic molecules is computationally costly. Spectroscopic signals can also be computed by combining the SQC/MM dynamics with the time-dependent non-perturbation approach.[110,111] However, this implementation is highly demanding for on-the-fly simulations: It requires a direct inclusion of the laser field into the Hamiltonian, and each time delay between the pulses requires a separate calculation.

In the present work, we propose a protocol in which the on-the-fly SQC/MM dynamics is combined with the DW methodology, and apply it for the simulation of TA PP spectra. In our protocol, the windowing scheme employed for the assignment of quantum states in the SQC/MM framework is used to define the currently occupied electronic state and to specify the transition dipole moment (TDM) between this state and the target state. This simplified treatment permits a convenient and efficient evaluation of the DW functions and provides an efficient and effective way to simulate TA PP signals on-the-fly.

It should be noted that Miller, Stock and their coworkers used the mapping approach in combination with the DW methodology for the calculation of time-resolved spectra for several model systems described by linear-vibronic-coupling Hamiltonians.[100,101,112] As distinct from these works, we develop the on-the-fly DW-MM methodology: The SQC scheme employed in the present work transforms the mapping variables back to the occupation numbers, which allows us to obtain simple explicit expressions for the DW functions which are convenient for the on-the-fly simulations. This largely extends the applicability of the on-the-fly SQC/MM-DW methodology, which can be used for the description of photoinduced dynamics and spectroscopic responses in realistic molecular systems. In this work, we simulate TA PP spectra of two popular molecular systems,[113] azobenzene[9] and cis-hepta-3,5,7-trieniminium cation (PSB4).[114]

2 Theoretical Methods and Computational Details

2.1 SQC/MM mapping

The SQC/MM method was implemented in the on-the-fy nonadiabatic dynamics simulation because of its excellent balance between computational costs and accuracy.[81,85] In this method, a quantum Hamiltonian with N discrete states is transformed into a mapping Hamiltonian with N coupled harmonic oscillators.[65] The replacement of quantum operators by the classical ones enables the implementation of the quasiclassical dynamics with the trajectory-adjusted zero point energy (ZPE) correction.[64,92] The "bin" technique is employed in the initial sampling and in the final assignment of quantum states. As is usually recommended, the triangle window technique[90] is employed in the present work.

2.1.1 MM Hamiltonian in the Adiabatic Representation

The classical MM Hamiltonian in the adiabatic representation reads

$$H = \frac{1}{2\mathbf{M}}\mathbf{P}_{kin}^2 + \sum_i^F \left[\frac{1}{2}(x_i)^2 + \frac{1}{2}(p_i)^2 - \gamma\right] V_i(\mathbf{R}). \tag{1}$$

The momentum $\mathbf{P}_{kin}$ is defined as

$$\mathbf{P}_{kin} = \mathbf{P} + \sum_{ij}^F (x_i p_j)\mathbf{d}_{ij}(\mathbf{R}), \tag{2}$$

where $\mathbf{R}$ and $\mathbf{P}$ are, respectively, coordinates and momenta of the nuclear DoFs. x_i and p_i are coordinates and momenta of the mapping electronic variables. i labels the electronic states, F is the total number of these states, $V_i(\mathbf{R})$ is the potential energy of i^{th} electronic state, γ denotes the ZPE correction and $\mathbf{d}_{ij}$ represents the first-order non-adiabatic coupling (NAC) vector.

The effective potential term

$$V_{eff}(\mathbf{R})) = \sum_i^F \frac{1}{2}(x_i^2 + p_i^2 - 2\gamma)V_i(\mathbf{R}), \tag{3}$$

is rearranged into the symmetrized form

$$V_{eff}(\mathbf{R})) = \frac{1}{F}\sum_i^F V_i(\mathbf{R}) + \frac{1}{F}\sum_{ij}^F \frac{1}{4}(x_i^2 + p_i^2 - x_j^2 - p_j^2)(V_i(\mathbf{R}) - V_j(\mathbf{R})), \tag{4}$$

which gives a better stability in the numerical propagation.

The classical equations of motion (EOMs) read:[95]

$$\begin{aligned}
\dot{x}_i &= p_i \frac{1}{F}\sum_j^F (V_i(\mathbf{R}) - V_j(\mathbf{R})) + \sum_j^F (x_j \mathbf{d}_{ji}(\mathbf{R})) \cdot \frac{\mathbf{P}_{kin}}{\mathbf{M}} \\
\dot{p}_i &= -x_i \frac{1}{F}\sum_j^F (V_i(\mathbf{R}) - V_j(\mathbf{R})) + \sum_j^F (p_j \mathbf{d}_{ji}(\mathbf{R})) \cdot \frac{\mathbf{P}_{kin}}{\mathbf{M}} \\
\dot{\mathbf{R}} &= \frac{\mathbf{P}_{kin}}{\mathbf{M}} \\
\dot{\mathbf{P}}_{kin} &= -\frac{\partial V_{eff}(\mathbf{R})}{\partial \mathbf{R}} + \frac{1}{2}\sum_{ij}^F (p_i p_j + x_i x_j)(V_j(\mathbf{R}) - V_i(\mathbf{R}))\mathbf{d}_{ji}(\mathbf{R}).
\end{aligned} \tag{5}$$

2.1.2 Symmetrical Triangle Window and Initial Sampling

In the SQC/MM dynamics, the window function is used to sample electronic DoFs initially and assign quantum states finally.[81,90] For multistate situations, the triangle window function is defined as[91]

$$W_i(\mathbf{n} = n_1, ...n_i, ...n_f) = w_1(n_i)\prod_{i\neq j}^F w_0(n_i, n_j), \tag{6}$$

where

$$w_1(n_i) = \begin{cases} (2-\gamma-n_i)^{2-F} & \text{for} \quad 1-\gamma < n_i < 2-\gamma \\ 0 & \text{otherwise} \end{cases} \tag{7}$$

and

$$w_0(n_i, n_j) = \begin{cases} 1 & \text{for} \quad n_j < 2-2\gamma-n_i \\ 0 & \text{otherwise} \end{cases} \tag{8}$$

meaning that $w_i = 1$ if the system stays in the i^{th} state, while $w_i = 0$ otherwise.

The action-angle sampling method generates the initial x_i^0 and p_i^0 in the i^{th} electronic state, *i.e.*

$$\begin{aligned}
x_i^0 &= \sqrt{2(n_i^0+\gamma)}\cos\theta \\
p_i^0 &= \sqrt{2(n_i^0+\gamma)}\sin\theta,
\end{aligned} \tag{9}$$

where n_i^0 is obtained by the sampling within the triangle window function and $\theta \in [-\pi, \pi]$.

For the final assignment, the triangle window function bins the action variables n_i into integers 0 or 1

$$n_i = \frac{1}{2}(x_i)^2 + \frac{1}{2}(p_i)^2 - \gamma. \tag{10}$$

2.1.3 Trajectory-Adjusted Electronic ZPE

Recently, Miller and Cotton introduced a trajectory-adjusted ZPE scheme, in which each trajectory uses its own ZPE correction for γ.[92] Once the electronic coordinates and momenta are sampled initially, the ZPE correction is defined by

$$\gamma_i = \frac{1}{2}(x_i^0)^2 + \frac{1}{2}(p_i^0)^2 - \delta_{ij}, \tag{11}$$

where j is the adiabatic electronic state in the initial sampling. Obviously, the value of the ZPE correction γ_i is different for each trajectory. With this trajectory-adjusted γ_i, the action variable of the electronic DoF is

$$n_i = \frac{1}{2}(x_i)^2 + \frac{1}{2}(p_i)^2 - \gamma_i \tag{12}$$

during the trajectory propagation.[92] Meanwhile, the MM Hamiltonian in the adiabatic representation is expressed in terms of the trajectory-adjusted γ_i as follows:

$$H = \frac{1}{2\boldsymbol{M}}\boldsymbol{P}_{kin}^2 + \sum_i^F \left[\frac{1}{2}(x_i)^2 + \frac{1}{2}(p_i)^2 + \gamma_i\right] E_i(\boldsymbol{R}). \tag{13}$$

More details on the trajectory-adjusted ZPE approach are found in Ref.[92]

2.2 Nonlinear Spectroscopic Signals

2.2.1 Third-Order Response

Let us consider a molecular system in an external field. The corresponding Hamiltonian reads

$$\hat{H}(t) = \hat{H}_M + \hat{H}_F(t), \tag{14}$$

where $\hat{H}_M$ is the molecular Hamiltonian and $\hat{H}_F(t)$ is the Hamiltonian describing the field-matter interactions. Explicitly,

$$\hat{H}_F(t) = -\hat{\boldsymbol{\mu}} \cdot \mathbf{E}(t), \tag{15}$$

where $\hat{\boldsymbol{\mu}}$ represents the TDM operator and $\mathbf{E}(t)$ denotes the total electric field of the laser pulses. Any spectroscopic signal is determined by the third-order polarization,

$$\mathbf{P}^{(3)}(t) = -i \int_0^\infty dt_3 \int_0^\infty dt_2 \int_0^\infty dt_1 \mathbf{E}(t-t_3)\mathbf{E}(t-t_3-t_2)\mathbf{E}(t-t_3-t_2-t_1) S^{(3)}(t_3,t_2,t_1), \tag{16}$$

which is specified by the convolution of the external field with the three-time NRF[35]

$$S^{(3)}(t_3,t_2,t_1) = Tr(\hat{\boldsymbol{\mu}}^I(t_1+t_2+t_3)[\hat{\boldsymbol{\mu}}^I(t_1+t_2),[\hat{\boldsymbol{\mu}}^I(t_1),[\hat{\boldsymbol{\mu}}^I(0),\hat{\rho}(-\infty)]]]). \tag{17}$$

Here

$$\hat{\boldsymbol{\mu}}^I(t) = e^{i\hat{H}_M(t)}\hat{\boldsymbol{\mu}}e^{-i\hat{H}_M(t)} \tag{18}$$

is the TDM operator in the Heisenberg representation and $\hat{\rho}(-\infty)$ is the equilibrium density operator of the molecular system before the arrival of the laser pulses. In the present work, we assume that

$$\hat{\rho}(-\infty) = |0\rangle\langle 0| \otimes |\nu_0\rangle\langle\nu_0|, \tag{19}$$

meaning that the system is initially in the electronic ground state $|0\rangle$ and in the vibrational ground state $|\nu_0\rangle$.

2.2.2 TA PP Spectra

In TA PP spectroscopy, the molecular system is prepared by the pump (pu) pulse and detected by the probe (pr) pulse,

$$\begin{aligned} \mathbf{E}(t) &= \mathbf{E}_{pu}(t) + \mathbf{E}_{pr}(t), \\ \mathbf{E}_{pu}(t) &= \boldsymbol{\epsilon}_{pu} A_{pu} E_{pu}(t) e^{i\mathbf{k}_{pu}\mathbf{x}} e^{-i\omega_{pu}t} + c.c., \\ \mathbf{E}_{pr}(t-\tau) &= \boldsymbol{\epsilon}_{pr} A_{pr} E_{pr}(t-\tau) e^{i\mathbf{k}_{pr}\mathbf{x}} e^{-i\omega_{pr}t} + c.c. \end{aligned} \tag{20}$$

Here τ is the time delay between the pulses, $\boldsymbol{\epsilon}_{pu}$ and $\boldsymbol{\epsilon}_{pr}$ are the unit vectors of the linear polarization of the pulses, A_{pu} and A_{pr} are the pulse amplitudes, $E_{pu}(t)$ and $E_{pr}(t)$ are the dimensionless envelope functions, $\mathbf{k}_{pu}$ and $\mathbf{k}_{pr}$ are the wave vectors and ω_{pu} and ω_{pr} are the pulse carrier frequencies.

The integral TA PP signal $I_{int}(\tau, \omega_{pr})$ is fully determined by the third-order polarization $P^{(3)}_{\mathbf{k}_{pr}}(\tau, t)$ in the phase-matching direction $\mathbf{k}_{pr}$[35]

$$I_{int}(\tau, \omega_{pr}) = \mathrm{Im}\ \omega_{pr} \int_{-\infty}^{\infty} dt E_{pr}(t) e^{i\omega_{pr}t} P^{(3)}_{\mathbf{k}_{pr}}(\tau, t). \tag{21}$$

2.2.3 Molecular Hamiltonian

The molecular Hamiltonian can be conveniently written in the block-diagonal form,

$$\hat{H}_M = \begin{pmatrix} \hat{H}_0 & \hat{H}_{0\mathrm{I}} & 0 \\ \hat{H}_{\mathrm{I}0} & \hat{H}_{\mathrm{I}} & 0 \\ 0 & 0 & \hat{H}_{\mathrm{II}} \end{pmatrix}. \tag{22}$$

Here $\hat{H}_0$ is the nuclear Hamiltonian in the electronic ground state 0, $\hat{H}_{\mathrm{I}}$ is the Hamiltonian governing the initial excitation and nonadiabatic dynamic in the lower-lying excited states, $\hat{H}_{\mathrm{II}}$ is the Hamiltonian describing vibronic dynamics in higher-lying states, while $\hat{H}_{0\mathrm{I}}$ and its Hermite conjugated $\hat{H}_{\mathrm{I}0}$ describe the NACs. The molecular electronic states fall into three manifolds 0, I and II according to their energies: I consists of the excited states interrogated via the pump pulse from the electronic ground state as well as of those states which are nonadiabatically coupled to them, while II includes the excited states accessible to the probe pulse from I.

The TDM operators can also be written as a sum of the rising and lowering operators,

$$\hat{\boldsymbol{\mu}} = \hat{\boldsymbol{\mu}}^{\uparrow} + \hat{\boldsymbol{\mu}}^{\downarrow}, \tag{23}$$

which, in turn, can be represented in the block-diagonal form

$$\hat{\boldsymbol{\mu}}^{\uparrow} = \begin{pmatrix} 0 & \hat{\boldsymbol{\mu}}_{0,\mathrm{I}} & 0 \\ 0 & 0 & \hat{\boldsymbol{\mu}}_{\mathrm{I},\mathrm{II}} \\ 0 & 0 & 0 \end{pmatrix}, \quad \hat{\boldsymbol{\mu}}^{\downarrow} = \begin{pmatrix} 0 & 0 & 0 \\ \hat{\boldsymbol{\mu}}_{\mathrm{I},0} & 0 & 0 \\ 0 & \hat{\boldsymbol{\mu}}_{\mathrm{II},\mathrm{I}} & 0 \end{pmatrix}. \tag{24}$$

Here $\hat{\boldsymbol{\mu}}_{0,\mathrm{I}}$ is responsible represents for transitions from the state 0 to the states of manifold I, etc. Within the rotating wave approximation (RWA), the matter-field interaction Hamiltonian assumes the form

$$\hat{\mathbf{H}}_F = -\hat{\boldsymbol{\mu}}^{\uparrow}\mathbf{E}_{RWA}(t) - \hat{\boldsymbol{\mu}}^{\downarrow}\mathbf{E}^*_{RWA}(t), \tag{25}$$

where

$$\mathbf{E}_{RWA}(t) = \mathbf{E}_{pu}(t) = \boldsymbol{\epsilon}_{pu} A_{pu} E_{pu}(t) e^{-i\mathbf{k}_{pu}\mathbf{x}} e^{i\omega_{pu}t} + \boldsymbol{\epsilon}_{pr} A_{pr} E_{pr}(t-\tau) e^{-i\mathbf{k}_{pr}\mathbf{x}} e^{i\omega_{pr}t}. \tag{26}$$

2.2.4 Quantum DW Approximation

The general TA PP signal defined per Eqs. (16) and (21) can be recast into the form suitable for on-the-fly simulations by performing a series of approximations.[60,115]

First, the quantum DW approximation is performed, which assumes that the pump and probe pulses are well separated, meaning that the time delay τ between the pulses is (much) longer than the pulse durations. Second, the short-pulse approximation is adopted, meaning that the nuclear dynamics during the pulse can be neglected. With these two assumptions, the integral TA PP signal takes the DW form

$$I_{int}(\tau,\omega_{pr}) = \omega_{pr}\mathrm{Tr}\left[\hat{D}(\omega_{pu})\left(e^{i\hat{H}_0\tau}\hat{W}_0(\omega_{pr})e^{-i\hat{H}_0\tau} + e^{i\hat{H}_I\tau}(\hat{W}_{\mathrm{I}}(\omega_{pr}) - \hat{W}_{\mathrm{II}}(\omega_{pr}))e^{-i\hat{H}_{\mathrm{I}}\tau}\right)\right], \tag{27}$$

where

$$\hat{D}(\omega_{pu}) = \int_{-\infty}^{\infty} dt_2^{'} \int_0^{\infty} dt_1 E_{pu}(t_2^{'})E_{pu}(t_2^{'} - t_1)e^{i\omega_{pu}t_1}e^{-i\hat{H}_{\mathrm{I}}t_1}\boldsymbol{\epsilon}_{pu}\boldsymbol{\mu}_{\mathrm{I},0}\hat{\rho}(-\infty)e^{i\hat{H}_0 t_1}\boldsymbol{\epsilon}_{pu}\boldsymbol{\mu}_{0,\mathrm{I}} + h.c. \tag{28}$$

is the doorway operator and

$$\begin{aligned}
\hat{W}_0(\omega_{pr}) &= \int_{-\infty}^{\infty} dt^{'} \int_0^{\infty} dt_3 E_{pr}(t^{'})E_{pr}(t^{'} + t_3)e^{i\omega_{pr}t_3}e^{i\hat{H}_0 t_3}\boldsymbol{\epsilon}_{pr}\boldsymbol{\mu}_{0,\mathrm{I}}e^{-i\hat{H}_{\mathrm{I}}t_3}\boldsymbol{\epsilon}_{pr}\boldsymbol{\mu}_{\mathrm{I},0} + h.c. \\
\hat{W}_I(\omega_{pr}) &= \int_{-\infty}^{\infty} dt^{'} \int_0^{\infty} dt_3 E_{pr}(t^{'})E_{pr}(t^{'} + t_3)e^{i\omega_{pr}t_3}\boldsymbol{\epsilon}_{pr}\boldsymbol{\mu}_{\mathrm{I},0}e^{i\hat{H}_0 t_3}\boldsymbol{\epsilon}_{pr}\boldsymbol{\mu}_{0,\mathrm{I}}e^{-i\hat{H}_{\mathrm{I}}t_3} + h.c. \\
\hat{W}_{\mathrm{II}}(\omega_{pr}) &= \int_{-\infty}^{\infty} dt^{'} \int_0^{\infty} dt_3 E_{pr}(t^{'})E_{pr}(t^{'} + t_3)e^{i\omega_{pr}t_3}\boldsymbol{\epsilon}_{pr}\boldsymbol{\mu}_{\mathrm{I},\mathrm{II}}e^{-i\hat{H}_{\mathrm{II}}t_3}\boldsymbol{\epsilon}_{pr}\boldsymbol{\mu}_{\mathrm{II},\mathrm{I}}e^{i\hat{H}_{\mathrm{I}}t_3} + h.c.
\end{aligned} \tag{29}$$

are the window operators. The terms proportional to $\hat{W}_0$, $\hat{W}_{\mathrm{I}}$ and $\hat{W}_{\mathrm{II}}$ in Eq. (27) yield the ground state bleach (GSB), stimulated emission (SE) and excited-state absorption (ESA) contributions to the total TA PP signal.

2.2.5 Quasiclassical DW Approximation

In the quasiclassical dynamics, the operators become functions in the nuclear phase space, and the trace turns into the integral over the nuclear phase space and the sum over the electronic states. Explicitly,

$$\begin{aligned}
I_{int}(\tau,\omega_{pr}) &= I_{int}^{GSB}(\tau,\omega_{pr}) + I_{int}^{SE}(\tau,\omega_{pr}) + I_{int}^{ESA}(\tau,\omega_{pr}) \\
I_{int}^{GSB}(\tau,\omega_{pr}) &= \omega_{pr}\sum_{e}\int d\mathbf{R}_g d\mathbf{P}_g D(\omega_{pu},\mathbf{R}_g,\mathbf{P}_g) W_0^{int}(\omega_{pu},\mathbf{R}_g(\tau),\mathbf{P}_g(\tau)) \\
I_{int}^{SE}(\tau,\omega_{pr}) &= \omega_{pr}\sum_{e}\int d\mathbf{R}_g d\mathbf{P}_g D(\omega_{pu},\mathbf{R}_g,\mathbf{P}_g) W_{\mathrm{I}}^{int}(\omega_{pu},\mathbf{R}_e(\tau),\mathbf{P}_e(\tau)) \\
I_{int}^{ESA}(\tau,\omega_{pr}) &= -\omega_{pr}\sum_{e}\int d\mathbf{R}_g d\mathbf{P}_g D(\omega_{pu},\mathbf{R}_g,\mathbf{P}_g) W_{\mathrm{II}}^{int}(\omega_{pu},\mathbf{R}_e(\tau),\mathbf{P}_e(\tau)),
\end{aligned} \tag{30}$$

where $\mathbf{R}_g$ and $\mathbf{P}_g$ represent the initial nuclear coordinates and momenta in the electronic ground state sampled according to the Wigner distribution $\rho_g^{Wig}(\mathbf{R}_g,\mathbf{P}_g)$, $\mathbf{R}_g(\tau)$ and $\mathbf{P}_g(\tau)$ denote the nuclear coordinates and momenta propagated in the electronic ground state up to $t=\tau$, and $\mathbf{R}_e(\tau)$ and $\mathbf{P}_e(\tau)$ denote the nuclear coordinates and momenta propagated up to $t=\tau$ in manifold I of the lower-lying excited electronic states. The quasiclassical doorway function reads

$$D(\omega_{pu},\mathbf{R}_g,\mathbf{P}_g) = |\boldsymbol{\epsilon}_{pu}\boldsymbol{\mu}_{ge}(\mathbf{R}_g)|^2 E_{pu}^2(\omega_{pu}-U_{eg}(\mathbf{R}_g))\rho_g^{Wig}(\mathbf{R}_g,\mathbf{P}_g), \tag{31}$$

and the quasiclassical window functions are defined as

$$\begin{aligned}
W_0^{int}(\omega_{pu},\mathbf{R}_g(\tau),\mathbf{P}_g(\tau)) &= \sum_{e}|\boldsymbol{\epsilon}_{pr}\boldsymbol{\mu}_{ge}(\mathbf{R}_g(\tau))|^2 E_{pr}^2(\omega_{pr}-U_{eg}(\mathbf{R}_g(\tau))), \\
W_{\mathrm{I}}^{int}(\omega_{pu},\mathbf{R}_e(\tau),\mathbf{P}_e(\tau)) &= |\boldsymbol{\epsilon}_{pr}\boldsymbol{\mu}_{ge(\tau)}(\mathbf{R}_e(\tau))|^2 E_{pr}^2(\omega_{pr}-U_{e(\tau)g}(\mathbf{R}_e(\tau))), \\
W_{\mathrm{II}}^{int}(\omega_{pu},\mathbf{R}_e(\tau),\mathbf{P}_e(\tau)) &= \sum_{f}|\boldsymbol{\epsilon}_{pr}\boldsymbol{\mu}_{e(\tau)f}(\mathbf{R}_e(\tau))|^2 E_{pr}^2(\omega_{pr}-U_{fe(\tau)}(\mathbf{R}_e(\tau))).
\end{aligned} \tag{32}$$

Here $E_{pu}(\omega)$ and $E_{pr}(\omega)$ are the Fourier transforms of $E_{pu}(t)$ and $E_{pr}(t)$, e represents the current lower-lying electronic state of manifold I, and f labels higher-lying electronic states of manifold II. $\boldsymbol{\mu}_{ge}$, $\boldsymbol{\mu}_{ge(\tau)}$ and $\boldsymbol{\mu}_{e(\tau)f}$ are the matrix elements of the TDMs operators between the corresponding electronic states, while $U_{eg}(\mathbf{R}_g(\tau))$, $U_{e(\tau)g}(\mathbf{R}_e(\tau))$ and $U_{fe(\tau)}(\mathbf{R}_e(\tau))$ are the transition frequencies (or, equivalently, energy gaps) between the corresponding electronic states. The notion $e(\tau)$ means that a trajectory initiated in an excited state e may jump into another electronic state.

The above derivations have been made under the assumption that NAC-induced transitions between manifolds 0, I, and II can be neglected on the timescale of interest. Once the internal conversion (IC) $e(\tau) \to g$ is allowed, Eq. (27) remains valid, but the window functions W_k^{int} defined per Eq. (32) have to be replaced by the new window functions $W_{k,\mathrm{IC}}^{int}$ which are defined in terms of the original window functions as follows:[115]

$$W_{0,\mathrm{IC}}^{int} = W_0^{int}, \tag{33}$$

$$W_{\mathrm{I,IC}}^{int} = \left[\begin{array}{ll} W_{\mathrm{I}}^{int}, & \text{if trajectory stays within } \{\mathrm{I}\} \\ -W_0^{int}, & \text{if trajectory jumps from } \{\mathrm{I}\} \text{ to } \{0\}, \end{array} \right. \tag{34}$$

$$W_{\mathrm{II,IC}}^{int} = \left[\begin{array}{ll} W_{\mathrm{II}}^{int}, & \text{if trajectory stays within } \{\mathrm{I}\} \\ 0, & \text{if trajectory jumps from } \{\mathrm{I}\} \text{ to } \{0\}. \end{array} \right. \tag{35}$$

If a trajectory jumps from manifold I back to the ground state, then $e(\tau)$ changes to g in Eq. (34). Owing to the $e(\tau) \to g$ IC, two GSB contributions arise: the cold and the hot. The cold contribution is the conventional GSB signal which reveals the nuclear wavepacket on the electronic ground state. It is described by the window function W_0^{int} of Eq. (33). The hot contribution is the IC-induced GSB signal, that reveals the manifold-I trajectory which jumps to the electronic ground state after the $e(\tau) \to g$ IC. This trajectory contributes to the GSB with a minus sign, $-W_0^{int}$ in Eq. (34).[115]

2.2.6 SCM/MM-DW Simulation Protocol

Cotton and Miller showed that the electronic part of the density matrix can be calculated within the SQC/MM framework by "binning" the trajectory to different windows which define the currently occupied electronic states in the mapping dynamics.[83,84] With this method, we obtain information about the involved electronic states and transitions and can straightforwardly evaluate the DW functions of Eqs. (31) and (32). Several comments are appropriate though. First, using the binning procedure to specify the DW functions correlates nicely with the central idea of the SQC/MM dynamics to use binning for defining the state occupations. Second, this method defines the active state in the trajectory propagation and only the diagonal elements of the density matrix are used to calculate the spectra. Therefore the current way to calculate the DW functions is very similar to that used in the on-the-fly TSH dynamics.[60,115,116] Third, we admit limitations of the current approach. In the applications of the present work, these limitations are not crucial, because manifold I contains just a single electronic state. For molecular systems with several simultaneously excited bright electronic states in manifold I, TA PP and other nonlinear spectroscopic signals will have contributions from electronic coherences between these electronic states. The SCM/MM approach can handle these coherences, and this will require the appropriate modification of the DW algorithm. Work in this direction is currently in progress.

With the current SCM/MM-DW methodology, we obtain the following simulation protocol.

Cold GSB signal.

1. Perform the initial sampling of the nuclear coordinates and momenta according to the Wigner distribution at the minimum of the ground-state potential energy surface and evaluate $D^{int}(\omega_{pu}, \mathbf{R}_g, \mathbf{P}_g)$.

2. Run the Born-Oppenheimer molecular-dynamics (BOMD) trajectories on the ground state and record electronic excitation energies and TDMs between the ground state and the states of manifold I.

3. Evaluate $W^{int}_{0,\mathrm{IC}}(\omega_{pr}, \mathbf{R}_g(\tau), \mathbf{P}_g(\tau))$ along the trajectory.

4. Average over all trajectories.

Hot GSB, SE, and ESA signals.

1. Initiate the dynamics in a specific state of manifold I. Sample electronic coordination and momenta in the excited state with the binning procedure and define the trajectory-

adjusted ZPE term. Perform the initial sampling of nuclear coordinates and momenta.

2. Propagate trajectories on the excited states. Store electronic and nuclear coordinates and momenta. Apply the binning procedure to electronic variables for the assignment of the quantum states. Save the excitation energies and TDMs in manifolds 0 and II along the trajectory in manifold I.

3. Calculate the $W^{int}_{0,\mathrm{IC}}(\omega_{pr}, \mathbf{R}_g(\tau), \mathbf{P}_g(\tau))$ when trajectories are binned to the ground state. Evaluate $W^{int}_{\mathrm{I,IC}}(\omega_{pr}, \mathbf{R}_e(\tau), \mathbf{P}_e(\tau))$ and $W^{int}_{\mathrm{II,IC}}(\omega_{pr}, \mathbf{R}_e(\tau), \mathbf{P}_e(\tau))$ when trajectories are binned to the excited state.

4. Average over all trajectories.

2.3 Computational Details

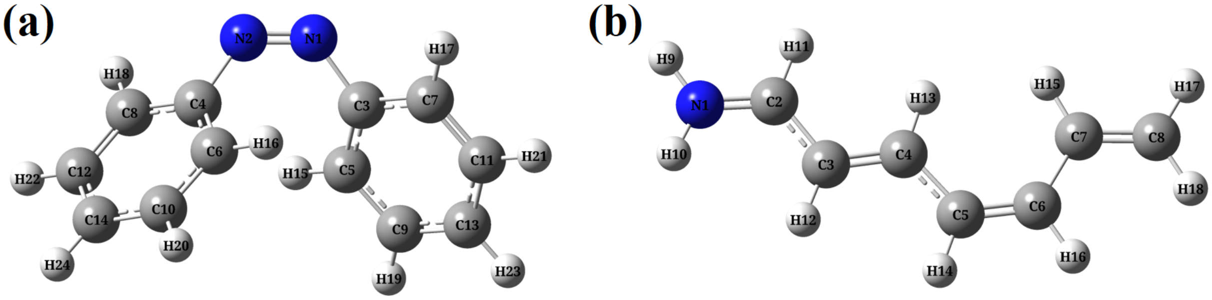

Figure 1: Molecular structure and labeling of atoms of (a) azobenzene and (b) PSB4.

To illustrate the performance of the SQC/MM-DW methodology, we chose two well-known molecules, *cis*-azobenzene and *cis*-hepta-3,5,7-trieniminium cation (PSB4), which are sketched in Fig. 1 (a) and (b). Optimizations of the S_0 minima of both systems were performed by employing the complete active space self-consistent field (CASSCF) in the Gaussian 16 package[117] where azobenzene is optimized at CASSCF(6,6)/6-31G level while PSB4 at CASSCF(8,8)/6-31G(d). In the on-the-fly SQC/MM dynamics simulations, the MOLPRO2022 package[118] was used for the electronic structures calculations.

For azobenzene, the SA6-CASSCF(6,6)/6-31G level of the electronic structure theory was used for both dynamics and spectroscopic calculations. For PSB4, the SA2-CASSCF(8,8)/6-

31G(d) level was used for the dynamics calculations, while the SA8-CASSCF(8,8)/6-31G(d) level at snapshots generated from the nonadiabatic dynamics simulations was used for the simulation of TA PP spectra.

Initial nuclear coordinates and momenta were generated by the Wigner sampling of the lowest vibrational level on the S_0 state. In the SQC/MM dynamics, the initial sampling and final assignment of quantum states for electronic DoFs were conducted using the symmetrical triangle window function with the trajectory-adjusted ZPE correction γ.[91,92] All electronic mapping coordinates and momenta were sampled by the action-angle method. The time steps for the propagation of the nuclear and electronic motions were 0.2 fs and 0.002 fs, respectively. All dynamics calculations were carried out with the JADE package.[94,119]

In azobenzene, manifold I contains a single state S_1 and manifold II consists of 4 states, from S_2 to S_5. In PSB4, manifold I also contains a single state S_1 and manifold II contains 6 states, from S_2 to S_7. 100 BOMD trajectories on the S_0 state were run up to 200 fs in the simulation of the GSB cold signal. Other 100 trajectories starting from the S_1 state were propagated to simulate the hot GSB, SE, and ESA signals. We chose snapshots per 10 steps from every trajectory to obtain the vertical excited energies (VEEs) and TDMs.

We chose Gaussian envelopes of the pump and probe pulses, $E_a(t) = \exp\{-(t/\tau_a)^2\}$ and $E_a(\omega) = \exp\{-(\omega\tau_a)^2/4\}$ (a = pu, pr), in which the pulse duration τ_a is set to 5 fs. This yields the pulse bandwidth 0.44 eV (full width at half maximum). In our simulations, polarization-sensitive effects and orientational averaging are not explicitly considered, which is equivalent to replacing the scalar products of the kind $|\boldsymbol{\epsilon}_{pu}\boldsymbol{\mu}_{ge}(\mathbf{R}_g)|^2$ by scalar coefficients $|\boldsymbol{\mu}_{ge}(\mathbf{R}_g)|^2$ in the DW functions. Within the DW formalism, the aforementioned effects can be taken care of as demonstrated in Ref.[120]

Considering isomerization of azobenzene and PSB4, we chose the following criterion to distinguish between the *cis* and *trans* photoproducts. If the dihedral angle falls within the range from -30 to 30 degrees between 175 and 200 fs, the product is of *cis*-structure. If the dihedral angle falls within the range of 150 to 210 degrees, the product is of *trans*-structure.

Specifically, the dihedrals C3-N1-N2-C1 and C4-C5-C6-C7 were chosen for azobenzene and PSB4, respectively (cf. Ref.[121]).

3 Results and Discussion

In these section we present the results of the on-the-fly simulations for azobenzene and PSB4. We systematically compare theoretical observables (evolutions of electronic populations, bond angles and lengths) and experimental observables (TA PP spectra), evaluated by using the DW-SQC/MM methodology.

While interpreting the TA PP spectra, it is useful to keep in mind that the SE and ESA contributions reflect the pump-pulse induced wavepacket motion in manifold I, projected on the electronic ground state (SE) or on the higher-lying electronic states of manifold II (ESA). The cold GSB signal mirrors the ground state wavepacket, while the hot GSB signal reveals the wavepacket initiated and propagated in manifold I but transferred to the electronic ground state after the IC.

3.1 Azobenzene

Photoisomerization of azobenzene finds a wide range of applications in high-density storage devices,[122,123] light-driven molecular motors[124,125] and protein probes.[126,127] Femtosecond spectroscopy revealed the important role of the low-lying excited states $n\pi^*$ and $\pi\pi^*$ in the course of isomerization.[12,128–130] From the theoretical perspective, azobenzene's nonadiabatic dynamics initiated in the $n\pi^*$ or $\pi\pi^*$ states were investigated extensively.[120,131–137]

Dynamical responses of azobenzene initiated in its lowest excited state S_1 are shown in Fig. 2. Panel (a) displays the S_1 (orange) and S_0 (blue) population evolution. Since the total, S_1+S_0, population is conserved, we concentrate on the S_1 population dynamics, which can be subdivided in several stages. The population remains constant within the first 25 fs. This establishes a characteristic time which the photoinduced wavepacket needs to travel

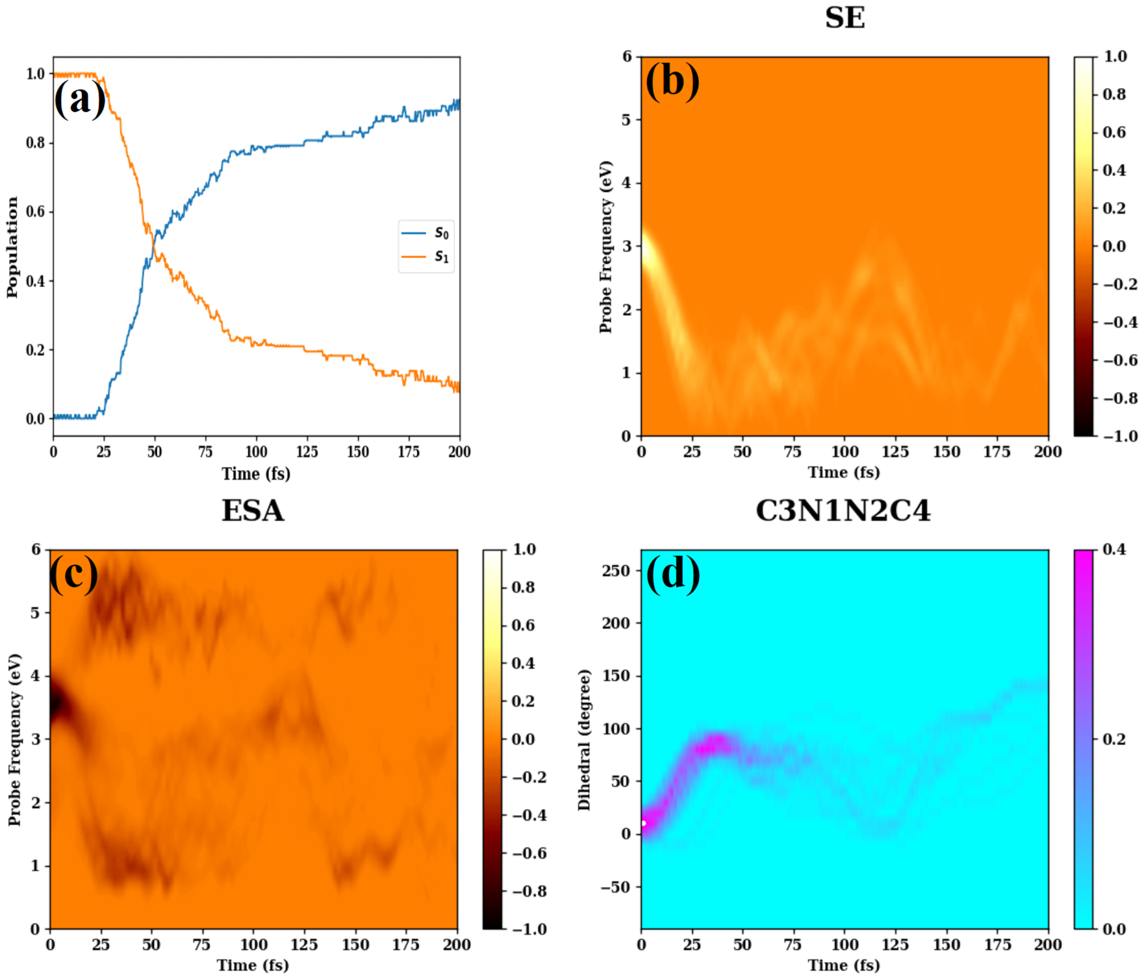

Figure 2: (a) Population dynamics of the S_0 and S_1 states of azobenzene, (b) normalized SE signal of azobenzene excited at $\omega_{pu} = 3.02$ eV vs the inter-pulse delay τ and the probe carrier frequency ω_{pr}, (c) normalized ESA signal of azobenzene, (d) normalized distribution of the C3-N1-N2-C4 torsional angle on the S_1 state vs the inter-pulse delay and the dihedral within $[-90, -270]$ degrees.

from the initial Franck-Condon region to the IC region. From 25 fs to 90 fs, the population exhibits a fast decay: S_1 looses half of its initial value at around 50 fs. Then the slower decay is observed.

Panels (b) and (c) demonstrate, respectively, the SE and ESA contributions to the integral TA PP spectrum. The central frequency of the pump laser is tuned into resonance with the $S_0 - S_1$ transition, $\omega_{pu} = 3.02$ eV. Initially, the SE spectrum in Fig. 2 (b) is concentrated in the vicinity of the Franck-Condon region ($\omega_{pr} \approx 3$ eV, which corresponds to the $S_0 - S_1$ VEE of Table S1. During the first 25 fs (when the S_1 population remains unchanged), the SE spectrum moves to the lower-frequency region and exhibits damped oscillations which are culminated in almost full recurrence around 120 fs.

The ESA spectrum in Fig. 2 (c) is initially concentrated around 3.6 eV, which corresponds to the $S_1 - S_4$ VEE in Table S1. At around 10 fs, the ESA spectrum splits into two components, of which the lower one oscillates around 1.0 eV and the upper one oscillates around 5.0 eV.

As the wavepacket moves away from the Franck-Condon region, both the SE and ESA signals exhibit significant quenching owing to the two main reasons. First, TDMs become smaller, which is a manifestation of the significance of the non-Condon effects in azobenzene.[115] Second, IC depopulates the the excited state. After 170 fs, the S_1 population becomes small and both the SE and ESA signals tend to vanish (see Fig. S5).

The time evolution of the SE and ESA spectra correlates with the torsional motion of the C3-N1-N2-C4 dihedral angle, as shown in Fig. 2 (d). The C3-N1-N2-C4 dihedral angle is around 5 degrees in the first 5 fs, indicating that the trajectories are near the S_0 minimum, and the SE and ESA maxima reveal the VEEs in the Franck-Condon region. Since the $S_1 - S_4$ TDM dominates the short-time dynamics, the ESA maximum coincides with the $S_1 - S_4$ VEE. The subsequent decrease of the $S_1 - S_4$ TDM and increase of the $S_1 - S_5$ and $S_1 - S_2$ TDMs lead to the splitting of the ESA signal. Interestingly, the time evolutions of the SE and ESA spectra correlate with those of the C3-N1-N2-C4 dihedrals in many aspects:

timescales, oscillation patterns, and so on. For example, maxima of the SE and ESA spectra around 120 fs in panels (b) and (c) correlate with the minimum of the dihedral angle in panel (d).

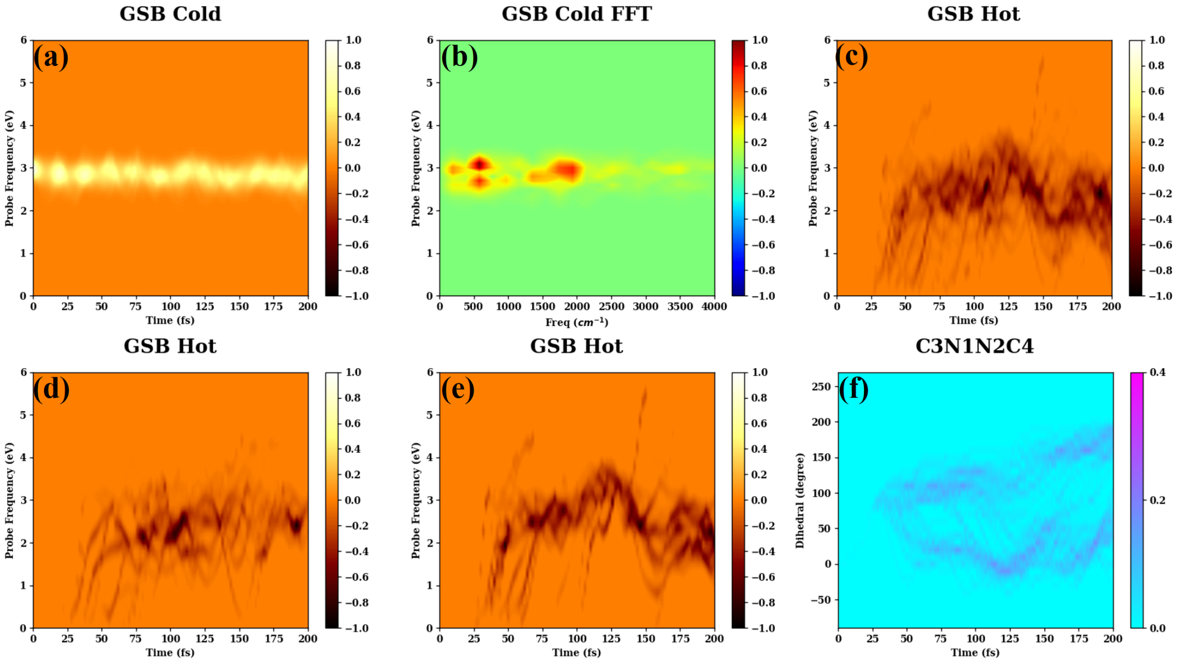

Figure 3: (a) Normalized cold GSB signal of azobenzene excited at $\omega_{pu} = 3.02$ eV vs the inter-pulse delay τ and the probe carrier frequency ω_{pr}, (b) normalized Fourier transform of the cold GSB signal, (c) normalized hot GSB signal of azobenzene, (d) normalized cold GSB signal corresponding to the final *trans*-azobenzene, (e) normalized GSB cold signal corresponding to the final *cis*-azobenzene, (f) normalized distribution of the C3-N1-N2-C4 torsional angle on the S_0 state vs τ and the dihedral angle within $[-90, -270]$ degrees.

Fig. 3 gives a multifaceted view of the GSB signal. The cold GSB signal is shown in Fig. 3 (a). It oscillates around 3.0 eV, revealing the $S_0 - S_1$ VEE in the Franck Condon region (Table S1). Inspired by the analyses of electronic two-dimensional spectra in terms of beating maps,[138–140] we show the Fourier transform of the cold GSB signal,

$$I_{int}^{GSB}(\omega, \omega_{pr}) = \mathrm{Re} \int dT e^{-i\omega T} I_{int}^{GSB}(T, \omega_{pr}), \tag{36}$$

in Fig. 3 (b). The figure reveals two peaks of vibrational origin: the first peak located around 2000 cm^{-1} (the period $\sim$ 17 fs) is attributed to the N=N stretch and the second peak located around 600 cm^{-1} (the period $\sim$ 56 fs) is attributed to the C-H out-of-plane motion. These two modes are assigned according to Table S5. Oscillations with a period of $\sim$ 17 fs are clearly seen in in Fig. 3 (b). Furthermore, since the first-peak frequency is roughly thrice larger than the second-peak frequency vibration, every forth peak of the cold GSB signal in panel (b) is more pronounced. Physically, the strong oscillation patterns in the cold GSB signal are a manifestation of the significant dependence of TDMs on nuclear coordinates (non-Condon effect). Fig. 3 (c) shows the hot GSB signal. It emerges at 25 fs, indicating the starting of IC. Then the hot GSB signal exhibits quite irregular oscillations which somewhat resemble those in the SE and ESA signals in Fig. 2 (b) and (c). For example, note a pronounced recurrence around 120 fs.

Two photoproducts, *trans*- and *cis*-isomers, are obtained after the photoexcitation of azobenzene. The two can be identified by monitoring the oscillatory patterns in the hot GSB signals. Fig. 3 (d) shows the hot GSB signal for the trajectories producing the *trans*-azobenzene. After 25 fs, the signal shifts to the blue following the torsional motion in panel (f). Then the signal remains in the domain around 3.0 eV, which is consistent with the behavior of the trajectories producing *trans*-azobenzene. The hot GSB signal in panel (e) is calculated for the trajectories producing *cis*-azobenzene. The first stage of its evolution is quite similar to that of its *trans*- counterpart, since both move to the blue following the torsional motion in panel (f). At longer times, however, a portion of trajectories producing the *cis*-signal returns to the low-energy domain. The reason is as follows: these trajectories experience further torsional motion after the *cis*-configuration is achieved. The *cis*-azobenzene has a stronger TDM to the excited states than the *trans*-azobenzene (see Tables S1 and S2). Hence the total hot GSB signal is dominated by the *cis*-azobenzene. Furthermore, the total hot GSB signal is quite erratic due to the excessive IC-induced vibrational motion.

Summarizing, the SE and ESA signals reveal the S_1 population dynamics and the C3-N1-N2-C4 torsion on the S_1 state. As the SE signal overlaps spectrally with the GSB signal (Fig. S1), the ESA signal is much easier to follow. The cold GSB signal gives information on the vibrational wavepacket motion on the S_0 state. The hot GSB signal reflects the C3-N1-N2-C4 torsion on the S_0 after IC. The *cis* and *trans* photoreaction channels may be distinguished by monitoring the hot GSB signals.

3.2 PSB4

The retinal protonated Schiff base (rPSB) is a chromophore of the rhodopsin family which is crucial for the vision process[141–143] and its ultrafast *cis-trans* photoisomerization is the key step for such biological functionality. The model systems protonated Schiff bases $CH_2(CH)_{2n\text{-}2}NH_2^+$ (PSBn) were often used to study photochemistry of rPSB.[121,144–147] Here, PSB4 was selected as a representative of PSBn.

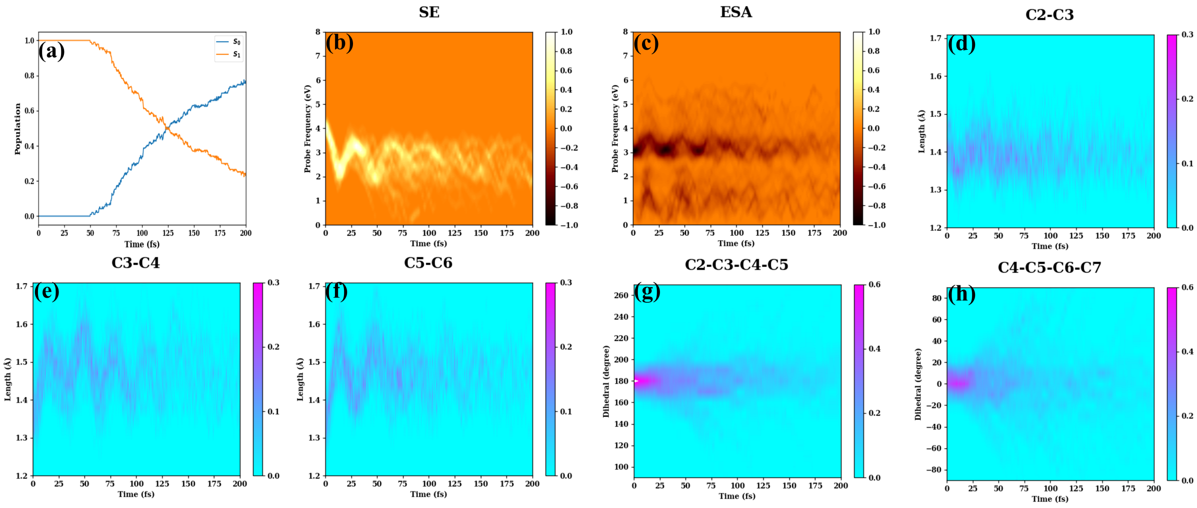

Figure 4: (a) Population dynamics of the S_0 and S_1 states of PSB4, (b) normalized SE signal of PSB4 versus the inter-pulse delay τ and the probe carrier frequency ω_{pr}. The pump frequency $\omega_{pu} = 4.09$ eV is resonant with the S_1 state. (c) normalized ESA signal of PSB4, (d) normalized distribution of the C2-C3 stretch on the S_1 state vs τ and the length within $[1.2, 1.7]$ Å, (e) normalized distribution of the C3-C4 stretch on the S_1 state, (f) normalized distribution of the C5-C6 stretch on the S_1 state, (g) normalized distribution of the C2-C3-C4-C5 torsion on the S_1 state vs τ and the dihedral angle within $[90, -270]$ degrees, (h) normalized distribution of the C4-C5-C6-C7 torsion on the S_1 state.

We begin our discussion with the S_1 and S_0 population evolutions presented in Fig. 4 (a). Similar to azobenzene and due to the same reasons, the nonadiabatic S_1 evolution starts with a delay. For PSB4, however, the delay is longer, around 50 fs, and the population decay is slower. Namely, the S_1 population of PSB4 halves at about 125 fs, and reaches some 20% of its initial value at 200 fs. Fig.4 displays the SE signal. It is located around 4 eV (which corresponds to the $S_0 - S_1$ VEE in Table S3) and exhibits pronounced slightly damped oscillations with a period of $\sim$ 30 fs. After 120 fs, the signal retains oscillatory behavior, but becomes more erratic and does not reveal a specific oscillation frequency. The ESA signal of Fig. 4 (c) shows a qualitatively similar behavior, but consists of two leading components: The upper component oscillating around 3.5 eV is produced by the $S_1 - S_4$ and $S_1 - S_5$ transitions, while the lower component oscillating around 1 eV corresponds to the $S_1 - S_2$ transition (Table S3). The ESA signal is governed by the stronger $S_1 - S_2$, $S_1 - S_4$ and $S_1 - S_5$ TDMs. The overall quenching of the SE and ESA signals after $\sim$ 50 fs correlates with the S_1 population decay. The SE/ESA evolution before $\sim$ 50 fs reflects the underdamped motion of the manifold I wavepacket.

To clarify which nuclear coordinates play a dominant role in the SE/ESA oscillatory dynamics, we plot evolutions of bond lengths for several internal coordinates, C2-C3, C3-C4, and C5-C6 in Fig. 4 (d), (e) and (f). Clearly, the C2-C3, C3-C4, and C5-C6 motions show the oscillatory patterns with a period of $\sim$ 30 fs which matches the SE and ESA oscillation periods. Furthermore, the overall intensity decays of the SE and ESA signals also correlate with the overall quenching of the bond lengths. This is reasonable, as these motions drive the wavepacket away from the Franck-Condon region with large TDMs. At the same time, this motion guides the system to the conical-intersection-driven IC region. This is the primary cause of the weakening of the SE and ESA signals (see Fig. S6). The dihedral angles for the coordinates C2-C3-C4-C5 and C4-C5-C6-C7 shown in Fig. 4 (g) and (h)) which are almost symmetric with respect to 180 and 0 degrees were also identified in Ref.[121]

Let us now turn to the GSB signals. The cold GSB signal in Fig. 5 (a) exhibits oscillates around 4.0 eV corresponding to the $S_0 - S_1$ VEE in Table S3. Fig. 5 (b), which shows the Fourier-transformed cold GSB signal defined per Eq. (36), exhibits three peaks located at 300 cm^{-1}, 1300 cm^{-1} and 1700 cm^{-1}. These frequencies correspond to the vibrational

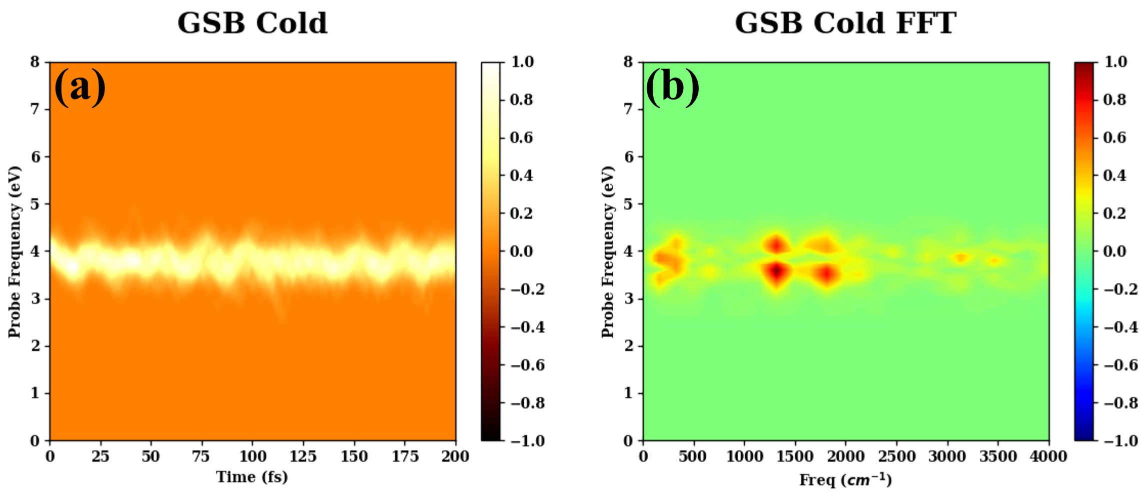

Figure 5: (a) Normalized GSB cold signal of PSB4 vs the inter-pulse delay τ and the probe carrier frequency ω_{pr} for $\omega_{pu} = 3.02$ eV chosen in resonance with the $S_0 - S_1$ VEE, (b) normalized Fourier transform of the cold GSB signal of PSB4.

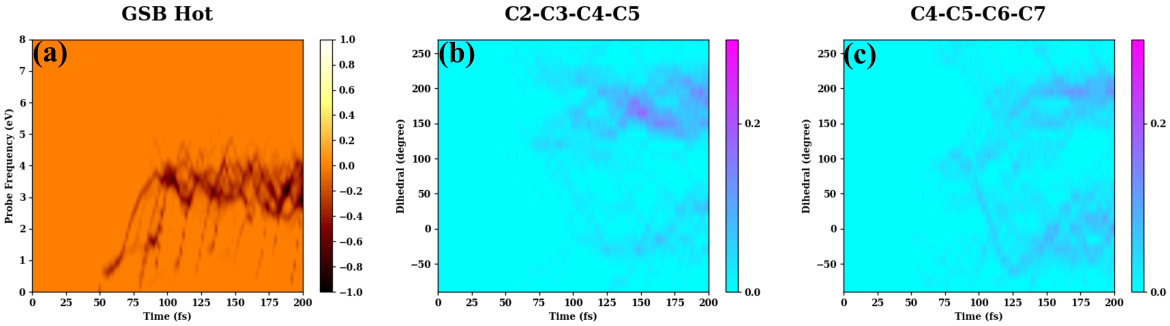

Figure 6: (a) Normalized hot GSB signal of PSB4 vs the inter-pulse delay τ and the probe carrier frequency ω_{pr} for $\omega_{pu} = 4.09$ eV chosen in resonance with the S_1 state, (b) normalized distribution of the C2-C3-C4-C5 torsion on the S_0 state vs τ and the dihedral angle within $[-90, -270]$ degrees, (c) normalized distribution of the C4-C5-C6-C7 torsion on the S_0.

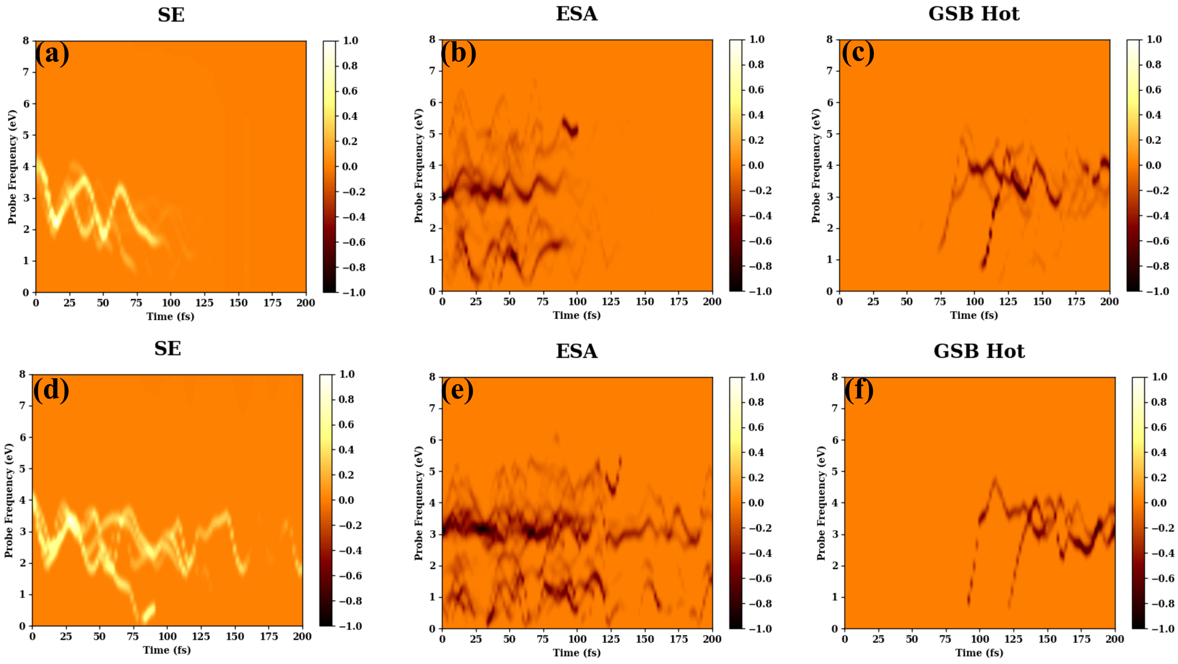

Figure 7: Normalized hot GSB (a), SE (b), and ESA (c) signals for the trajectories ending in the *trans*-PSB4. Normalized hot GSB (d), SE (e), and ESA (f) signals for the trajectories ending in the *cis*-PSB4.

periods of 111 fs, 26 fs, and 20 fs, respectively. They are attributed to the torsion of the $C_5{=}C_6$ bond, the waging of the C−C−H or N−C−H modes, and the stretching motion of the C=C bonds, which are assigned according to Table S6. The three vibrational modes are responsible for the GSB dynamics in Fig. 5 (a): the second and the third mode produce oscillations while the first one causes a slight increase of the oscillation amplitude around ~ 100 fs.

Fig. 6 (a) illustrates the hot GSB signal. The hot high-energy IC-driven wavepacket enters the ground state around 50 fs. It exhibits a high-amplitude motion which manifests itself through erratic oscillations of the hot GSB signal spanning around 3 eV in the frequency domain. Due to the excessive energy, the wavepacket experiences quite complicated dynamics, so that a trajectory moving towards, say, *cis*-PSB4 may go over the barrier and reach *trans*-PSB4 (and the other way around). This statement is corroborated by Figs. 6 (b) and (c), which demonstrate that the torsional trajectories started at almost the same point bifurcate and follow multiple crisscrossing pathways towards the final products. Since vibrational relaxation and dissipation are not accounted for in simulations, it is quite tricky to estimate the final branching ratio of the products. However, as we discussed previously, the $C_5{=}C_6$ torsional motion is of primarily importance in the wavepacket evolution. We thus tried to divide all trajectories according to the dihedral angle of this bond. The results are shown in Fig. 7, which displays the SE, ESA, and hot GSB spectra corresponding to the *trans* (upper panels) and *cis* (lower panels) isomers. The trajectories leading to the *trans*-isomer move towards the conical intersection and experience IC. Thus the corresponding SE (a) and ESA (b) signals disappear at 125 fs. The trajectories towards the *cis*-isomer bifurcate. Many of them bypass the conical intersection and continue to stay on the excited state. Obviously, these trajectories require more time to return to the conical intersection region, and the corresponding SE (d) and ESA (e) signals live longer. A smaller fraction of the trajectories do directly reaches the conical intersection, and produces short-lived branches of the SE (d) and ESA (e) signals. As for hot GSB signals in panels (c) and (f), they look qualitatively very similar and do not allow us to distinguish between the two isomers.

We thus conclude that the carbon skeleton stretch on the S_1 state and several torsional motions are manifested in the SE and ESA spectra, the intensity of which correlates with the S_1 population decay. Importantly, both of these signals are clearly discernible in the total TA PP signal (see Fig. S1) – the only signal which is detectable experimentally. Hence, TA PP spectroscopy can conveniently monitor photoisomerization pathways and distinguish between *cis* and *trans* PSB4 products.

3.3 Conclusion

We developed a novel protocol for the simulation of TA PP signals which is based on combining the on-the-fly SQC/MM dynamical framework and the DW representation of nonlinear spectroscopy. The DW approximation rests on the assumption that the pump and probe pulses are temporally well separated and are short on the dynamical timescale of interest. The DW-SQC/MM TA PP signals depend exclusively on the classical analogues of the TDMs operators and electronic energies, and explicit propagation of the system dynamics in the presence of laser fields are avoided. The developed simulation protocol can be straightforwardly extended to other mapping schemes and to other nonlinear spectroscopic signals.

The methodology has been tested and illustrated by the ab initio evaluation of TA PP spectra of realistic molecular systems, azobenzene and the PSB4. For both molecules, the SE and ESA spectra were demonstrated to give a direct fingerprint of the excited state wavepacket dynamics and permit the monitoring of the isomerization pathways en route to the final photoproducts.

At the moment, the ab initio DW methodology has been combined with three most popular quasiclassical trajectory simulation protocols: TSH (including Tully's fewest switches method,[115,116,120] Landau-Zenner method,[60,148] and machine-learning enhanced Landau-Zenner method[149]), Ehrenfest,[150] and SQC/MM in the present work. In this context, two comments are in order. For the molecular systems with a single excited electronic state, the DW methodology results in the computational protocol which is essentially the same for all three (semi)classical methods. Hence, the differences in the predictions of the spectroscopic signals can be directly pinned down to the differences in the approximations used in a specific dynamical method. For molecular systems with several bright excited electronic states, TA PP and other nonlinear spectroscopic signals will have contributions from electronic coherences. In this latter case, different variants of the mapping approach may have advantages over the TSH and Ehrenfest counterparts.[64] This latter argument may broaden the applicability of spectroscopic DW simulations performed with SQC/MM and other variants of the mapping approach.

Acknowledgement

This work is supported by NSFC projects (No. 22333003, 22361132528, and 21933011). The authors thank the Supercomputing Center, Computer Network Information Center, and

Chinese Academy of Sciences. M.F.G. acknowledges support from the NSFC project No. 22373028.

References

(1) Domcke, W.; Yarkony, D.; Köppel, H. *Conical intersections: electronic structure, dynamics & spectroscopy*; World Scientific, 2004; Vol. 15.

(2) Domcke, W.; Yarkony, D. R.; Köppel, H. *Conical intersections: theory, computation and experiment*; World Scientific, 2011; Vol. 17.

(3) Cheng, Y.-C.; Fleming, G. R. Dynamics of light harvesting in photosynthesis. *Annual Review of Physical Chemistry* **2009**, *60*, 241–262.

(4) Chenu, A.; Scholes, G. D. Coherence in energy transfer and photosynthesis. *Annual Review of Physical Chemistry* **2015**, *66*, 69–96.

(5) Clayton, R. K. *Photosynthesis: physical mechanisms and chemical patterns*; Cambridge University Press, 1980; Vol. 4.

(6) Jankowiak, R.; Reppert, M.; Zazubovich, V.; Pieper, J.; Reinot, T. Site selective and single complex laser-based spectroscopies: a window on excited state electronic structure, excitation energy transfer, and electron–phonon coupling of selected photosynthetic complexes. *Chemical Reviews* **2011**, *111*, 4546–4598.

(7) Beckstead, A. A.; Zhang, Y.; de Vries, M. S.; Kohler, B. Life in the light: nucleic acid photoproperties as a legacy of chemical evolution. *Physical Chemistry Chemical Physics* **2016**, *18*, 24228–24238.

(8) Kohler, B. Nonradiative decay mechanisms in DNA model systems. *The Journal of Physical Chemistry Letters* **2010**, *1*, 2047–2053.

(9) Bandara, H. D.; Burdette, S. C. Photoisomerization in different classes of azobenzene. *Chemical Society Reviews* **2012**, *41*, 1809–1825.

(10) Martinez, T. J. Insights for light-driven molecular devices from ab initio multiple spawning excited-state dynamics of organic and biological chromophores. *Accounts of Chemical Research* **2006**, *39*, 119–126.

(11) Vukovic, L.; Burmeister, C. F.; Kral, P.; Groenhof, G. Control mechanisms of photoisomerization in protonated Schiff bases. *The Journal of Physical Chemistry Letters* **2013**, *4*, 1005–1011.

(12) Lednev, I. K.; Ye, T.-Q.; Hester, R. E.; Moore, J. N. Femtosecond time-resolved UV- visible absorption spectroscopy of trans-azobenzene in solution. *The Journal of Physical Chemistry* **1996**, *100*, 13338–13341.

(13) Zewail, A. H. Femtochemistry. *The Journal of Physical Chemistry* **1993**, *97*, 12427–12446.

(14) Suzuki, T. Femtosecond time-resolved photoelectron imaging. *Annual Review of Physical Chemistry.* **2006**, *57*, 555–592.

(15) Tamai, N.; Miyasaka, H. Ultrafast dynamics of photochromic systems. *Chemical Reviews* **2000**, *100*, 1875–1890.

(16) Kumpulainen, T.; Lang, B.; Rosspeintner, A.; Vauthey, E. Ultrafast Elementary Photochemical Processes of Organic Molecules in Liquid Solution. *Chemical Reviews* **2017**, *117*, 10826–10939.

(17) Gross, N.; Kuhs, C. T.; Ostovar, B.; Chiang, W.-Y.; Wilson, K. S.; Volek, T. S.; Faitz, Z. M.; Carlin, C. C.; Dionne, J. A.; Zanni, M. T.; others Progress and prospects in optical ultrafast microscopy in the visible spectral region: Transient absorption

and two-dimensional microscopy. *The Journal of Physical Chemistry C* **2023**, *127*, 14557–14586.

(18) Pollard, W. T.; Mathies, R. A. Analysis of femtosecond dynamic absorption spectra of nonstationary states. *Annual Review of Physical Chemistry* **1992**, *43*, 497–523.

(19) Walbrun, Z. S.; Wong, C. Y. In situ measurement of evolving excited-state dynamics during deposition and processing of organic films by single-shot transient absorption. *Annual Review of Physical Chemistry* **2023**, *74*, 267–286.

(20) Maiuri, M.; Garavelli, M.; Cerullo, G. Ultrafast spectroscopy: State of the art and open challenges. *Journal of the American Chemical Society* **2019**, *142*, 3–15.

(21) Seel, M.; Domcke, W. Femtosecond time-resolved ionization spectroscopy of ultrafast internal-conversion dynamics in polyatomic molecules: Theory and computational studies. *The Journal of Chemical Physics* **1991**, *95*, 7806–7822.

(22) Mukamel, S. Multidimensional femtosecond correlation spectroscopies of electronic and vibrational excitations. *Annual Review of Physical Chemistry* **2000**, *51*, 691–729.

(23) Gelin, M. F.; Egorova, D.; Domcke, W. Efficient calculation of time-and frequency-resolved four-wave-mixing signals. *Accounts of Chemical Research* **2009**, *42*, 1290–1298.

(24) Ginsberg, N. S.; Cheng, Y.-C.; Fleming, G. R. Two-dimensional electronic spectroscopy of molecular aggregates. *Accounts of Chemical Research* **2009**, *42*, 1352–1363.

(25) Tanimura, Y.; Mukamel, S. Two-dimensional femtosecond vibrational spectroscopy of liquids. *The Journal of Chemical Physics* **1993**, *99*, 9496–9511.

(26) Dougherty, T. P.; Wiederrecht, G. P.; Nelson, K. A.; Garrett, M. H.; Jensen, H. P.;

Warde, C. Femtosecond resolution of soft mode dynamics in structural phase transitions. *Science* **1992**, *258*, 770–774.

(27) Loring, R. F. Calculating multidimensional optical spectra from classical trajectories. *Annual Review of Physical Chemistry* **2022**, *73*, 273–297.

(28) Brida, D.; Tomasello, G.; Orlandi, G.; Kukura, P.; Mathies, R. A.; Garavelli, M.; Cerullo, G. Conical Intersection Dynamics of the Primary Photoisomerization Event in Vision. *Nature* **2010**, *467*, 440–443.

(29) Conti, I.; Cerullo, G.; Nenov, A.; Garavelli, M. Ultrafast spectroscopy of photoactive molecular systems from first principles: Where we stand today and where we are going. *Journal of the American Chemical Society* **2020**, *142*, 16117–16139.

(30) Yan, Y.; Liu, Y.; Xing, T.; Shi, Q. Theoretical Study of Excitation Energy Transfer and Nonlinear Spectroscopy of Photosynthetic Light- Harvesting Complexes Using the Nonperturbative Reduced Dynamics Method. *WIREs Computational Molecular Science* **2021**, *11*, e1498.

(31) Jansen, T. L. Computational spectroscopy of complex systems. *The Journal of Chemical Physics* **2021**, *155*, 170901.

(32) Gelin, M. F.; Chen, L.; Domcke, W. Equation-of-motion methods for the calculation of femtosecond time-resolved 4-wave-mixing and N-wave-mixing signals. *Chemical Reviews* **2022**, *122*, 17339–17396.

(33) Krumland, J.; Guerrini, M.; De Sio, A.; Lienau, C.; Cocchi, C. Two-dimensional electronic spectroscopy from first principles. *Applied Physics Reviews* **2024**, *11*, 011305.

(34) Faraji, S.; Picconi, D.; Palacino-González, E. Advanced quantum and semiclassical methods for simulating photoinduced molecular dynamics and spectroscopy. *WIREs Computational Molecular Science* **2024**, *14*, e1731.

(35) Mukamel, S. *Principles of Nonlinear Optical Spectroscopy*; Oxford series in optical and imaging sciences; Oxford University Press, 1995.

(36) Yan, Y. J.; Fried, L. E.; Mukamel, S. Ultrafast pump-probe spectroscopy: femtosecond dynamics in Liouville space. *The Journal of Physical Chemistry* **1989**, *93*, 8149–8162.

(37) Pollard, W. T.; Lee, S.-Y.; Mathies, R. A. Wave packet theory of dynamic absorption spectra in femtosecond pump–probe experiments. *The Journal of Chemical Physics* **1990**, *92*, 4012–4029.

(38) Wang, H.; Thoss, M. Multilayer formulation of the multiconfiguration time-dependent Hartree theory. *The Journal of Chemical Physics* **2003**, *119*, 1289–1299.

(39) Wang, H. Multilayer multiconfiguration time-dependent Hartree theory. *The Journal of Physical Chemistry A* **2015**, *119*, 7951–7965.

(40) Gelin, M. F.; Borrelli, R. Simulation of Nonlinear Femtosecond Signals at Finite Temperature via Thermo Field Dynamics - Tensor Train Method: General Theory and Application to Time- and Frequency-Resolved Fluorescence of the Fenna-Matthews-Olson Complex. *Journal of Chemical Theory and Computation* **2021**, *17*, 4316–4331.

(41) Shi, Q.; Chen, L.; Nan, G.; Xu, R.-X.; Yan, Y. Efficient hierarchical Liouville space propagator to quantum dissipative dynamics. *The Journal of Chemical Physics* **2009**, *130*, 084105.

(42) May, V.; Kühn, O. *Charge and energy transfer dynamics in molecular systems*; John Wiley & Sons, 2023.

(43) Tanaka, M.; Tanimura, Y. Quantum dissipative dynamics of electron transfer reaction system: Nonperturbative hierarchy equations approach. *Journal of the Physical Society of Japan* **2009**, *78*, 073802–073802.

(44) Tanimura, Y. Numerically "Exact" Approach to Open Quantum Dynamics: The Hierarchical Equations of Motion (HEOM). *The Journal of Chemical Physics* **2020**, *153*, 020901.

(45) Tully, J. C. Perspective: Nonadiabatic dynamics theory. *The Journal of Chemical Physics* **2012**, *137*, 22A301.

(46) Subotnik, J. E.; Jain, A.; Landry, B.; Petit, A.; Ouyang, W.; Bellonzi, N. Understanding the surface hopping view of electronic transitions and decoherence. *Annual Review of Physical Chemistry* **2016**, *67*, 387–417.

(47) Persico, M.; Granucci, G. An overview of nonadiabatic dynamics simulations methods, with focus on the direct approach versus the fitting of potential energy surfaces. *Theoretical Chemistry Accounts* **2014**, *133*, 1–28.

(48) Kapral, R. Progress in the theory of mixed quantum-classical dynamics. *Annual Review of Physical Chemistry.* **2006**, *57*, 129–157.

(49) Curchod, B. F.; Martínez, T. J. Ab initio nonadiabatic quantum molecular dynamics. *Chemical Reviews* **2018**, *118*, 3305–3336.

(50) Tully, J. C. Molecular dynamics with electronic transitions. *The Journal of Chemical Physics* **1990**, *93*, 1061–1071.

(51) Golubev, N. V.; Begušić, T.; Vaníček, J. On-the-fly ab initio semiclassical evaluation of electronic coherences in polyatomic molecules reveals a simple mechanism of decoherence. *Physical Review Letters* **2020**, *125*, 083001.

(52) Barbatti, M. Nonadiabatic dynamics with trajectory surface hopping method. *Wiley Interdisciplinary Reviews: Computational Molecular Science* **2011**, *1*, 620–633.

(53) Crespo-Otero, R.; Barbatti, M. Recent advances and perspectives on nonadiabatic mixed quantum–classical dynamics. *Chemical Reviews* **2018**, *118*, 7026–7068.

(54) Matsika, S. Electronic structure methods for the description of nonadiabatic effects and conical intersections. *Chemical Reviews* **2021**, *121*, 9407–9449.

(55) Mai, S.; González, L. Molecular photochemistry: recent developments in theory. *he Journal of Chemical Physics andte Chemie International Edition* **2020**, *59*, 16832–16846.

(56) Wang, L.; Akimov, A.; Prezhdo, O. V. Recent progress in surface hopping: 2011–2015. *The Journal of Physical Chemistry Letters* **2016**, *7*, 2100–2112.

(57) Zimmermann, T.; Vaníček, J. Efficient on-the-fly ab initio semiclassical method for computing time-resolved nonadiabatic electronic spectra with surface hopping or Ehrenfest dynamics. *The Journal of Chemical Physics* **2014**, *141*, 134102.

(58) Kowalewski, M.; Fingerhut, B. P.; Dorfman, K. E.; Bennett, K.; Mukamel, S. Simulating coherent multidimensional spectroscopy of nonadiabatic molecular processes: From the infrared to the x-ray regime. *Chemical Reviews* **2017**, *117*, 12165–12226.

(59) Fingerhut, B. P.; Dorfman, K. E.; Mukamel, S. Monitoring nonadiabatic dynamics of the RNA base uracil by UV pump–IR probe spectroscopy. *The Journal of Physical Chemistry Letters* **2013**, *4*, 1933–1942.

(60) Gelin, M. F.; Huang, X.; Xie, W.; Chen, L.; Doslic, N.; Domcke, W. Ab initio surface-hopping simulation of femtosecond transient-absorption pump–probe signals of nonadiabatic excited-state dynamics using the doorway–window representation. *Journal of Chemical Theory and Computation* **2021**, *17*, 2394–2408.

(61) Jaeger, H. M.; Fischer, S.; Prezhdo, O. V. Decoherence-induced surface hopping. *The Journal of Chemical Physics* **2012**, *137*, 22A545.

(62) Wang, Z.; Dong, J.; Wang, L. Large-scale surface hopping simulation of charge trans-

port in hexagonal molecular crystals: role of electronic coupling signs. *Journal of Physics: Condensed Matter* **2023**, *35*, 345401.

(63) Qiu, J.; Lu, Y.; Wang, L. Multilayer subsystem surface hopping method for large-scale nonadiabatic dynamics simulation with hundreds of thousands of states. *Journal of Chemical Theory and Computation* **2022**, *18*, 2803–2815.

(64) Stock, G.; Thoss, M. Classical description of nonadiabatic quantum dynamics. *Advances in Chemical Physics* **2005**, *131*, 243–375.

(65) Meyer, H.-D.; Miller, W. H. A classical analog for electronic degrees of freedom in nonadiabatic collision processes. *The Journal of Chemical Physics* **1979**, *70*, 3214–3223.

(66) Thoss, M.; Stock, G. Mapping approach to the semiclassical description of nonadiabatic quantum dynamics. *Physical Review A* **1999**, *59*, 64.

(67) Li, B.; Miller, W. H. A Cartesian classical second-quantized many-electron Hamiltonian, for use with the semiclassical initial value representation. *The Journal of Chemical Physics* **2012**, *137*, 154107.

(68) Liu, J. A unified theoretical framework for mapping models for the multi-state Hamiltonian. *The Journal of Chemical Physics* **2016**, *145*, 204105.

(69) Liu, J.; He, X.; Wu, B. Unified formulation of phase space mapping approaches for nonadiabatic quantum dynamics. *Accounts of Chemical Research* **2021**, *54*, 4215–4228.

(70) He, X.; Cheng, X.; Wu, B.; Liu, J. Nonadiabatic Field with Triangle Window Functions on Quantum Phase Space. *The Journal of Physical Chemistry Letters* **2024**, *15*, 5452–5466.

(71) Wu, B.; He, X.; Liu, J. Nonadiabatic Field on Quantum Phase Space: A Century after Ehrenfest. *The Journal of Physical Chemistry Letters* **2024**, *15*, 644–658.

(72) Cheng, X.; He, X.; Liu, J. A novel class of phase space representations for the exact population dynamics of two-state quantum systems and the relation to triangle window functions. *Chinese Journal of Chemical Physics* **2024**, *37*, 230–254.

(73) Shi, Q.; Geva, E. Semiclassical theory of vibrational energy relaxation in the condensed phase. *The Journal of Physical Chemistry A* **2003**, *107*, 9059–9069.

(74) Hu, D.; Ying, W.; Huo, P. Resonance enhancement of vibrational polariton chemistry obtained from the mixed quantum-classical dynamics simulations. *The Journal of Physical Chemistry Letters* **2023**, *14*, 11208–11216.

(75) Mulvihill, E.; Gao, X.; Liu, Y.; Schubert, A.; Dunietz, B. D.; Geva, E. Combining the mapping Hamiltonian linearized semiclassical approach with the generalized quantum master equation to simulate electronically nonadiabatic molecular dynamics. *The Journal of Chemical Physics* **2019**, *151*, 074103.

(76) Saller, M. A.; Kelly, A.; Richardson, J. O. On the identity of the identity operator in nonadiabatic linearized semiclassical dynamics. *The Journal of Chemical Physics* **2019**, *150*, 071101.

(77) Kelly, A.; Van Zon, R.; Schofield, J.; Kapral, R. Mapping quantum-classical Liouville equation: Projectors and trajectories. *The Journal of Chemical Physics* **2012**, *136*, 084101.

(78) Tao, G. Electronically nonadiabatic dynamics in complex molecular systems: An efficient and accurate semiclassical solution. *The Journal of Physical Chemistry A* **2013**, *117*, 5821–5825.

(79) Stock, G.; Thoss, M. Semiclassical description of nonadiabatic quantum dynamics. *Physical Review Letters* **1997**, *78*, 578.

(80) Cotton, S. J.; Miller, W. H. Symmetrical windowing for quantum states in quasi-classical trajectory simulations. *The Journal of Physical Chemistry A* **2013**, *117*, 7190–7194.

(81) Cotton, S. J.; Miller, W. H. Symmetrical windowing for quantum states in quasi-classical trajectory simulations. *The Journal of Physical Chemistry A* **2013**, *117*, 7190–7194.

(82) Cotton, S. J.; Miller, W. H. A symmetrical quasi-classical spin-mapping model for the electronic degrees of freedom in non-adiabatic processes. *The Journal of Physical Chemistry A* **2015**, *119*, 12138–12145.

(83) Miller, W. H.; Cotton, S. J. Classical molecular dynamics simulation of electronically non-adiabatic processes. *Faraday Discussions* **2016**, *195*, 9–30.

(84) Miller, W. H.; Cotton, S. J. Communication: Wigner functions in action-angle variables, Bohr-Sommerfeld quantization, the Heisenberg correspondence principle, and a symmetrical quasi-classical approach to the full electronic density matrix. *The Journal of Chemical Physics* **2016**, *145*, 081102.

(85) Cotton, S. J.; Miller, W. H. Symmetrical windowing for quantum states in quasi-classical trajectory simulations: Application to electronically non-adiabatic processes. *The Journal of Chemical Physics* **2013**, *139*, 234112.

(86) Xie, Y.; Zheng, J.; Lan, Z. Performance evaluation of the symmetrical quasi-classical dynamics method based on Meyer-Miller mapping Hamiltonian in the treatment of site-exciton models. *The Journal of Chemical Physics* **2018**, *149*, 174105.

(87) Provazza, J.; Coker, D. F. Communication: Symmetrical quasi-classical analysis of linear optical spectroscopy. *The Journal of Chemical Physics* **2018**, *148*, 181102.

(88) Gao, X.; Saller, M. A.; Liu, Y.; Kelly, A.; Richardson, J. O.; Geva, E. Benchmarking quasiclassical mapping Hamiltonian methods for simulating electronically nonadiabatic molecular dynamics. *Journal of Chemical Theory and Computation* **2020**, *16*, 2883–2895.

(89) Jain, A.; Subotnik, J. E. Vibrational energy relaxation: A benchmark for mixed quantum–classical methods. *The Journal of Physical Chemistry A* **2018**, *122*, 16–27.

(90) Cotton, S. J.; Miller, W. H. A new symmetrical quasi-classical model for electronically non-adiabatic processes: Application to the case of weak non-adiabatic coupling. *The Journal of Chemical Physics* **2016**, *145*, 144108.

(91) Cotton, S. J.; Miller, W. H. A symmetrical quasi-classical windowing model for the molecular dynamics treatment of non-adiabatic processes involving many electronic states. *The Journal of Chemical Physics* **2019**, *150*, 104101.

(92) Cotton, S. J.; Miller, W. H. Trajectory-adjusted electronic zero point energy in classical Meyer-Miller vibronic dynamics: Symmetrical quasiclassical application to photodissociation. *The Journal of Chemical Physics* **2019**, *150*, 194110.

(93) Gao, X.; Geva, E. Improving the accuracy of quasiclassical mapping Hamiltonian methods by treating the window function width as an adjustable parameter. *The Journal of Physical Chemistry A* **2020**, *124*, 11006–11016.

(94) Hu, D.; Xie, Y.; Peng, J.; Lan, Z. On-the-fly symmetrical quasi-classical dynamics with Meyer–Miller mapping Hamiltonian for the treatment of nonadiabatic dynamics at conical intersections. *Journal of Chemical Theory and Computation* **2021**, *17*, 3267–3279.

(95) Cotton, S. J.; Liang, R.; Miller, W. H. On the adiabatic representation of Meyer-Miller electronic-nuclear dynamics. *The Journal of Chemical Physics* **2017**, *147*, 064112.

(96) Mandal, A.; Yamijala, S. S.; Huo, P. Quasi-diabatic representation for nonadiabatic dynamics propagation. *Journal of Chemical Theory and Computation* **2018**, *14*, 1828–1840.

(97) Tang, D.; Fang, W.-H.; Shen, L.; Cui, G. Combining Meyer–Miller Hamiltonian with electronic structure methods for on-the-fly nonadiabatic dynamics simulations: implementation and application. *Physical Chemistry Chemical Physics* **2019**, *21*, 17109–17117.

(98) Talbot, J. J.; Head-Gordon, M.; Cotton, S. J. The symmetric quasi-classical model using on-the-fly time-dependent density functional theory within the Tamm–Dancoff approximation. *Molecular Physics* **2023**, *121*, e2153761.

(99) Zhou, W.; Mandal, A.; Huo, P. Quasi-diabatic scheme for nonadiabatic on-the-fly simulations. *The Journal of Physical Chemistry Letters* **2019**, *10*, 7062–7070.

(100) Stock, G.; Miller, W. H. A classical model for time-and frequency-resolved spectroscopy of nonadiabatic excited-state dynamics. *Chemical Physics Letters* **1992**, *197*, 396–404.

(101) Stock, G.; Miller, W. H. Classical formulation of the spectroscopy of nonadiabatic excited-state dynamics. *The Journal of Chemical Physics* **1993**, *99*, 1545–1555.

(102) Uspenskiy, I.; Strodel, B.; Stock, G. Classical calculation of transient absorption spectra monitoring ultrafast electron transfer processes. *Journal of Chemical Theory and Computation* **2006**, *2*, 1605–1617.

(103) Uspenskiy, I.; Strodel, B.; Stock, G. Classical description of the dynamics and time-

resolved spectroscopy of nonadiabatic cis–trans photoisomerization. *Chemical Physics* **2006**, *329*, 109–117.

(104) Van Der Vegte, C.; Dijkstra, A.; Knoester, J.; Jansen, T. Calculating two-dimensional spectra with the mixed quantum-classical ehrenfest method. *The Journal of Physical Chemistry A* **2013**, *117*, 5970–5980.

(105) Tempelaar, R.; Van Der Vegte, C. P.; Knoester, J.; Jansen, T. L. Surface hopping modeling of two-dimensional spectra. *he Journal of Chemical Physics* **2013**, *138*, 164106.

(106) Provazza, J.; Segatta, F.; Garavelli, M.; Coker, D. F. Semiclassical path integral calculation of nonlinear optical spectroscopy. *Journal of Chemical Theory and Computation* **2018**, *14*, 856–866.

(107) Provazza, J.; Segatta, F.; Coker, D. F. Modeling nonperturbative field-driven vibronic dynamics: Selective state preparation and nonlinear spectroscopy. *Journal of Chemical Theory and Computation* **2020**, *17*, 29–39.

(108) Sun, X. Hybrid equilibrium-nonequilibrium molecular dynamics approach for two-dimensional solute-pump/solvent-probe spectroscopy. *The Journal of Chemical Physics* **2019**, *151*, 194507.

(109) Karsten, S.; Ivanov, S. D.; Bokarev, S. I.; Kühn, O. Quasi-classical approaches to vibronic spectra revisited. *The Journal of Chemical Physics* **2018**, *148*, 102337.

(110) Gao, X.; Lai, Y.; Geva, E. Simulating absorption spectra of multiexcitonic systems via quasiclassical mapping Hamiltonian methods. *Journal of Chemical Theory and Computation* **2020**, *16*, 6465–6480.

(111) Gao, X.; Geva, E. A nonperturbative methodology for simulating multidimensional spectra of multiexcitonic molecular systems via quasiclassical mapping Hamiltonian methods. *Journal of Chemical Theory and Computation* **2020**, *16*, 6491–6502.

(112) Uspenskiy, I.; Strodel, B.; Stock, G. Classical calculation of transient absorption spectra monitoring ultrafast electron transfer processes. *Journal of Chemical Theory and Computation* **2006**, *2*, 1605–1617.

(113) Dugave, C.; Demange, L. Cis- trans isomerization of organic molecules and biomolecules: implications and applications. *Chemical Reviews* **2003**, *103*, 2475–2532.

(114) Gozem, S.; Luk, H. L.; Schapiro, I.; Olivucci, M. Theory and simulation of the ultrafast double-bond isomerization of biological chromophores. *Chemical Reviews* **2017**, *117*, 13502–13565.

(115) Xu, C.; Lin, K.; Hu, D.; Gu, F. L.; Gelin, M. F.; Lan, Z. Ultrafast internal conversion dynamics through the on-the-Fly simulation of transient absorption pump–probe spectra with different electronic structure methods. *The Journal of Physical Chemistry Letters* **2022**, *13*, 661–668.

(116) Hu, D.; Peng, J.; Chen, L.; Gelin, M. F.; Lan, Z. Spectral fingerprint of excited-state energy transfer in dendrimers through polarization-sensitive transient-absorption pump–probe signals: On-the-fly nonadiabatic dynamics simulations. *The Journal of Physical Chemistry Letters* **2021**, *12*, 9710–9719.

(117) Frisch, M. J.; Trucks, G. W.; Schlegel, H. B.; Scuseria, G. E.; Robb, M. A.; Cheeseman, J. R.; Scalmani, G.; Barone, V.; Petersson, G. A.; Nakatsuji, H.; Li, X.; Caricato, M.; Marenich, A. V.; Bloino, J.; Janesko, B. G.; Gomperts, R.; Mennucci, B.; Hratchian, H. P.; Ortiz, J. V.; Izmaylov, A. F.; Sonnenberg, J. L.; Williams-Young, D.; Ding, F.; Lipparini, F.; Egidi, F.; Goings, J.; Peng, B.; Petrone, A.; Henderson, T.; Ranasinghe, D.; Zakrzewski, V. G.; Gao, J.; Rega, N.; Zheng, G.; Liang, W.; Hada, M.; Ehara, M.; Toyota, K.; Fukuda, R.; Hasegawa, J.; Ishida, M.; Nakajima, T.; Honda, Y.; Kitao, O.; Nakai, H.; Vreven, T.; Throssell, K.; Montgomery, J. A., Jr.; Peralta, J. E.; Ogliaro, F.; Bearpark, M. J.; Heyd, J. J.; Broth-

ers, E. N.; Kudin, K. N.; Staroverov, V. N.; Keith, T. A.; Kobayashi, R.; Normand, J.; Raghavachari, K.; Rendell, A. P.; Burant, J. C.; Iyengar, S. S.; Tomasi, J.; Cossi, M.; Millam, J. M.; Klene, M.; Adamo, C.; Cammi, R.; Ochterski, J. W.; Martin, R. L.; Morokuma, K.; Farkas, O.; Foresman, J. B.; Fox, D. J. Gaussian˜16 Revision C.01. 2016; Gaussian Inc. Wallingford CT.

(118) Werner, H.-J.; Knowles, P. J.; Manby, F. R.; Black, J. A.; Doll, K.; Heßelmann, A.; Kats, D.; Köhn, A.; Korona, T.; Kreplin, D. A.; others The Molpro quantum chemistry package. *The Journal of Chemical Physics* **2020**, *152*, 144107.

(119) Du, L.; Lan, Z. An on-the-fly surface-hopping program jade for nonadiabatic molecular dynamics of polyatomic systems: implementation and applications. *Journal of Chemical Theory and Computation* **2015**, *11*, 1360–1374.

(120) Xu, C.; Lin, C.; Peng, J.; Zhang, J.; Lin, S.; Gu, F. L.; Gelin, M. F.; Lan, Z. On-the-fly simulation of time-resolved fluorescence spectra and anisotropy. *The Journal of Chemical Physics* **2024**, *160*, 104109.

(121) Szymczak, J. J.; Barbatti, M.; Lischka, H. Is the photoinduced isomerization in retinal protonated Schiff bases a single-or double-torsional process? *The Journal of Physical Chemistry A* **2009**, *113*, 11907–11918.

(122) Liu, Z. F.; Hashimoto, K.; Fujishima, A. Photoelectrochemical information storage using an azobenzene derivative. *Nature* **1990**, *347*, 658–660.

(123) Rasmussen, P. H.; Ramanujam, P.; Hvilsted, S.; Berg, R. H. A remarkably efficient azobenzene peptide for holographic information storage. *Journal of the American Chemical Society* **1999**, *121*, 4738–4743.

(124) Norikane, Y.; Tamaoki, N. Light-driven molecular hinge: a new molecular machine showing a light-intensity-dependent photoresponse that utilizes the trans- cis isomerization of azobenzene. *Organic Letters* **2004**, *6*, 2595–2598.

(125) Muraoka, T.; Kinbara, K.; Aida, T. Mechanical twisting of a guest by a photoresponsive host. *Nature* **2006**, *440*, 512–515.

(126) Kim, Y.; Phillips, J. A.; Liu, H.; Kang, H.; Tan, W. Using photons to manipulate enzyme inhibition by an azobenzene-modified nucleic acid probe. *Proceedings of the National Academy of Sciences* **2009**, *106*, 6489–6494.

(127) Banghart, M. R.; Mourot, A.; Fortin, D. L.; Yao, J. Z.; Kramer, R. H.; Trauner, D. Photochromic blockers of voltage-gated potassium channels. *he Journal of Chemical Physics andte Chemie International Edition* **2009**, *48*, 9097–9101.

(128) Nägele, T.; Hoche, R.; Zinth, W.; Wachtveitl, J. Femtosecond photoisomerization of cis-azobenzene. *Chemical Physics Letters* **1997**, *272*, 489–495.

(129) Lednev, I.; Ye, T.-Q.; Matousek, P.; Towrie, M.; Foggi, P.; Neuwahl, F.; Umapathy, S.; Hester, R.; Moore, J. N. Femtosecond time-resolved UV-visible absorption spectroscopy of trans-azobenzene: dependence on excitation wavelength. *Chemical Physics Letters* **1998**, *290*, 68–74.

(130) Quick, M.; Dobryakov, A.; Gerecke, M.; Richter, C.; Berndt, F.; Ioffe, I.; Granovsky, A.; Mahrwald, R.; Ernsting, N.; Kovalenko, S. Photoisomerization dynamics and pathways of trans-and cis-azobenzene in solution from broadband femtosecond spectroscopies and calculations. *The Journal of Physical Chemistry B* **2014**, *118*, 8756–8771.

(131) Ciminelli, C.; Granucci, G.; Persico, M. The photoisomerization mechanism of azobenzene: A semiclassical simulation of nonadiabatic dynamics. *Chemistry–A European Journal* **2004**, *10*, 2327–2341.

(132) Pederzoli, M.; Pittner, J.; Barbatti, M.; Lischka, H. Nonadiabatic molecular dynamics study of the cis–trans photoisomerization of azobenzene excited to the S 1 state. *The Journal of Physical Chemistry A* **2011**, *115*, 11136–11143.

(133) Merritt, I. C.; Jacquemin, D.; Vacher, M. cis→ trans photoisomerisation of azobenzene: a fresh theoretical look. *Physical Chemistry Chemical Physics* **2021**, *23*, 19155–19165.

(134) Tang, D.; Shen, L.; Fang, W.-H. Evaluation of mixed quantum–classical molecular dynamics on cis-azobenzene photoisomerization. *Physical Chemistry Chemical Physics* **2021**, *23*, 13951–13964.

(135) Liang, R. First-Principles Nonadiabatic Dynamics Simulation of Azobenzene Photodynamics in Solutions. *Journal of Chemical Theory and Computation* **2021**, *17*, 3019–3030.

(136) Böckmann, M.; Doltsinis, N. L.; Marx, D. Unraveling a chemically enhanced photoswitch: bridged azobenzene. *he Journal of Chemical Physics andte Chemie International Edition* **2010**, *122*, 3454–3456.

(137) Wu, D.; Wang, Y.-T.; Fang, W.-H.; Cui, G.; Thiel, W. QM/MM Studies on Photoisomerization Dynamics of Azobenzene Chromophore Tethered to a DNA Duplex: Local Unpaired Nucleobase Plays a Crucial Role. *Chemistry–An Asian Journal* **2018**, *13*, 780–784.

(138) Butkus, V.; Valkunas, L.; Abramavicius, D. Molecular vibrations-induced quantum beats in two-dimensional electronic spectroscopy. *The Journal of Chemical Physics* **2012**, *137*, 044513.

(139) Butkus, V.; Zigmantas, D.; Valkunas, L.; Abramavicius, D. Vibrational vs. Electronic coherences in 2D spectrum of molecular systems. *Chemical Physics Letters* **2012**, *545*, 40–43.

(140) Zhan, S.; Gelin, M. F.; Huang, X.; Sun, K. Ab initio simulation of peak evolutions and beating maps for electronic two-dimensional signals of a polyatomic chromophore. *The Journal of Chemical Physics* **2023**, *158*, 194106.

(141) Schoenlein, R. W.; Peteanu, L. A.; Mathies, R. A.; Shank, C. V. The first step in vision: femtosecond isomerization of rhodopsin. *Science* **1991**, *254*, 412–415.

(142) Kukura, P.; McCamant, D. W.; Yoon, S.; Wandschneider, D. B.; Mathies, R. A. Structural observation of the primary isomerization in vision with femtosecond-stimulated Raman. *Science* **2005**, *310*, 1006–1009.

(143) Olivucci, M.; Tran, T.; Worth, G. A.; Robb, M. A. Unlocking the double bond in protonated Schiff bases by coherent superposition of S1 and S2. *The Journal of Physical Chemistry Letters* **2021**, *12*, 5639–5643.

(144) Zhang, X.; Herbert, J. M. Nonadiabatic dynamics with spin-flip vs linear-response time-dependent density functional theory: A case study for the protonated Schiff base C5H6NH2+. *The Journal of Chemical Physics* **2021**, *155*, 124111.

(145) Barneschi, L.; Kaliakin, D.; Huix-Rotllant, M.; Ferré, N.; Filatov, M.; Olivucci, M. Assessment of the Electron Correlation Treatment on the Quantum-Classical Dynamics of Retinal Protonated Schiff Base Models: XMS-CASPT2, RMS-CASPT2, and REKS Methods. *Journal of Chemical Theory and Computation* **2023**, *19*, 8189–8200.

(146) Toldo, J. M.; Mattos, R. S.; Pinheiro Jr, M.; Mukherjee, S.; Barbatti, M. Recommendations for Velocity Adjustment in Surface Hopping. *Journal of Chemical Theory and Computation* **2024**, *20*, 614–624.

(147) Huang, H.; Peng, J.; Zhang, Y.; Gu, F. L.; Lan, Z.; Xu, C. The development of the QM/MM interface and its application for the on-the-fly QM/MM nonadiabatic dynamics in JADE package: Theory, implementation, and applications. *The Journal of Chemical Physics* **2024**, *160*, 234101.

(148) Huang, X.; Xie, W.; Doslic, N.; Gelin, M. F.; Domcke, W. Ab initio quasiclassical simulation of femtosecond time-resolved two-dimensional electronic spectra of pyrazine. *The Journal of Physical Chemistry Letters* **2021**, *12*, 11736–11744.

(149) Pios, S. V.; Gelin, M. F.; Ullah, A.; Dral, P. O.; Chen, L. Artificial-Intelligence-Enhanced On-the-Fly Simulation of Nonlinear Time-Resolved Spectra. *The Journal of Physical Chemistry Letters* **2024**, *15*, 2325–2331.

(150) Perez-Castillo, R.; Freixas, V. M.; Mukamel, S.; Martinez-Mesa, A.; Uranga-Piña, L.; Tretiak, S.; Gelin, M. F.; Fernandez-Alberti, S. Transient-absorption spectroscopy of dendrimers via nonadiabatic excited-state dynamics simulations. *Chemical Science* **2024**, *15*, 13250–13261.

TOC Graphic

Some journals require a graphical entry for the Table of Contents. This should be laid out "print ready" so that the sizing of the text is correct.

Inside the `tocentry` environment, the font used is Helvetica 8 pt, as required by *Journal of the American Chemical Society*.

The surrounding frame is 9 cm by 3.5 cm, which is the maximum permitted for *Journal of the American Chemical Society* graphical table of content entries. The box will not resize if the content is too big: instead it will overflow the edge of the box.

This box and the associated title will always be printed on a separate page at the end of the document.